On the Sources and Sizes of Error in Predicting the Arrival Time of Interplanetary Coronal Mass Ejections using Global MHD Models

Pete Riley[1] **and Michal Ben-Nun**[1]

[1]Predictive Science Inc., San Diego, USA

Key Points:

- Errors in the arrival time of ICMEs derive from a mixture of individual, but identifiable uncertainties in the chain from the Sun to 1 AU
- Different ADAPT realizations produce errors in the arrival time of ICMEs of ±7 hours or more.
- Targeted studies aimed at reducing each of the uncertainties would improve the accuracy and precision in the arrival time of ICMEs

Corresponding author: Pete Riley, pete@predsci.com

Abstract

Accurate predictions of the properties of interplanetary coronal mass ejection (ICME)-driven disturbances are a key objective for space weather forecasts. The ICME's time of arrival (ToA) at Earth is an important parameter, and one that is amenable to a variety of modeling approaches. Previous studies suggest that the best models can predict the arrival time to within an absolute error of 10-15 hours. Here, we investigate the main sources of error in predicting a CME's ToA at Earth. These can be broken into two main categories: (1) the initial properties of the ejecta, including its speed, mass, and direction of propagation; and (2) the properties of the ambient solar wind into which it propagates. To estimate the relative contribution to ToA errors, we construct a set of numerical experiments of cone-model CMEs, where we vary the initial speed, mass, and direction at the inner radial boundary. Additionally, we build an ensemble of 12 ambient solar wind solutions using realizations from the ADAPT model. We find that each component in the chain contributes between ±2.5 and ±7 hours of uncertainty to the estimate of the CME's ToA. Importantly, different realizations of the synoptic produce the largest errors. This suggests that estimates of ToA will continue to be plagued with intrinsic errors of ±10 hours until tighter constraints can be found for these boundary conditions. Our results suggest that there are clear benefits to focused investigations aimed at reducing the uncertainties in CME speed, mass, direction, and input boundary magnetic fields.

Plain Language Summary

Coronal mass ejections are huge explosions of plasma and magnetic field, which, if they impact the EarthâĂŹs protective magnetospheric shield, can result in a range of consequences, from increased radiation doses for aircraft passengers to electrical blackouts across large regions. Being able to forecast their properties, as well as when they will arrive at Earth are key objectives for space weather programs. In this study, we have investigated a broad set of uncertainties associated with these predictions, which include the initial specification of the properties of the CME at the Sun as well as the properties of the interplanetary medium into which it propagates. Remarkably, and disappointingly, we find that there are inherent limitations in the accuracy of the forecasts that will not likely be resolved by more sophisticated modeling techniques. Instead, they will require substantial investment in developing more comprehensive datasets to drive the models, which, in turn, will require new space missions. More modest improvements, however, can be made by addressing components in the forecasting system and attempting to reduce (or at least accurately assess) the errors associated with them.

1 Introduction

Geomagnetic storms are an essential component of space weather at Earth, and anticipating their onset is one of the major priorities for the National Oceanic and Atmospheric Administration (NOAA) Space Weather Prediction Center (SWPC). The two primary drivers of these storms are fast solar wind streams and coronal mass ejections (CMEs). CMEs are large-scale coronal eruptions that propel plasma and magnetic fields into the solar wind, and are generally responsible for the most severe storms [*Gosling et al.*, 1990]. To provide one- to four-day warning of these storms, NOAA/SWPC operationally implemented the Wang-Sheeley-Arge-ENLIL cone model, or WSA+ENLIL [*Pizzo et al.*, 2011].

Ideally, a comprehensive CME forecasting framework would begin at the Sun, using first-principles models [e.g., *Forbes and Lin*, 2000], and provide the longest lead-time for predictions. However, in practice, models capable of mimicking the eruption of the CME and its evolution in the corona remain idealised and the subject of fundamental research, not operational forecasting [*Török et al.*, 2018]. Thus, current forecasting models blend elements of empiricism and domain reduction to provide tractable solutions. For example,

CMEs are often treated as hydrodynamic "pulses", usually inserted high in the corona, with properties inferred from relevant observations [e.g., *Riley et al.*, 2003; *Odstrcil et al.*, 2004].

The WSA+ENLIL forecasting system is a good example of the general approach applied by a number of groups [*Riley et al.*, 2018], and proceeds in the following manner: Magnetic maps of the solar magnetic field in the photosphere, obtained from ground- and/or space-based observatories [*Riley et al.*, 2014], are used to compute potential field models of the solar corona. An empirical prescription for the solar wind speed based on magnetic field structure, the Wang-Sheeley-Arge (WSA) model [*Arge et al.*, 2003], is used to specify boundary conditions for the ENLIL magnetohydrodynamic (MHD) model of the solar wind [*Odstrcil et al.*, 2003]. ENLIL is integrated in time until a steady-state background solar wind solution is reached beyond 1 AU. This solution is typically updated several times a day, as new magnetograms are made available. When observed, "cone-model" CMEs are injected into the flow and tracked out to 1 AU [e.g., *Pizzo et al.*, 2011].

Several previous studies have investigated the WSA+ENLIL forecasting system. *Pizzo et al.* [2015], for example, explored the effects of launching a range of cone-model CMEs into different idealized ambient solar wind states. In particular, they developed a set of idealised numerical experiments, propagating a series of CME pulses into (1) a uniform (spherically symmetric background); and (2) tilted-dipole stream structure. They found relatively predictable patterns in the time of arrival (ToA) of ICMEs as a function of the initial properties of the ejecta, and ruled out the possibility of any chaotic behaviour that might manifest itself in the forecasts.

Mays et al. [2015] developed ensemble model results for 35 observed CME events occurring between January 2013 and July 2014. For those events that were predicted to arrive at earth (17 events), they estimated the MAE error in ToA prediction of 12.3 hours. They also estimated correct and false-alarm ratios for these events. They suggested that the accuracy of the predicted arrival time was sensitive to the initial distribution of CME parameters, and that for their analyses, the spread was probably underestimated.

Riley et al. [2018] summarized a large number of CME forecasting tools and compared their forecasting capabilities with one another. They addressed: (1) How well the models predicted the arrival time of CME-driven shocks at Earth? (2) What were the errors associated with these forecasts? (3) Which, if any models performed better? and (4) Did any of the models had demonstrate improvements in accuracy over the six-year period that they had been in use? They found that, for the best models, CME-shock arrival times could be predicted with ± 1 hour (mean error) or ± 13 hours (mean absolute error), with a precision (standard deviation) of 15 hours. However, they also inferred that there had been no measurable improvement in model accuracy during the six-year interval that predictions had been made.

In this study, we build upon these earlier investigations in several important ways. First, we consider the propagation of CME pulses through a set of 12 ADAPT-GONG realizations of the photospheric magnetic field. These are estimates of the synchronic field that are, in principle all likely to be equally valid, or at least consistent with the available observations. Second, we consider the propagation of a large number of CME pulses that are representative of a fast CME with a distribution in properties that are consistent with the likely uncertainties in their measured values. Third, we estimate the contributions to the estimated errors in arrival time due to each component (or model parameter) in the modeled system.

2 Methods

2.1 Data

For this study, we use ADAPT-GONG quasi-synchronic magnetograms [*Arge et al.*, 2010]. These are âĂIJquasi-âĂİ or âĂIJpseudo-âĂİ synchronic in the sense that only observations from Earth-based solar observatories are used to generate each map at each point in time, and photospheric magnetic flux transport processes are invoked to evolve the magnetic field distribution as it drifts westward and beyond the observation window. Additionally, data assimilation techniques are used to update the modelled flux with new observations. In principle, this can account for both model and observational uncertainties, and, importantly, allows for the generation of multiple realizations at each point in time. For the purposes of computing MHD solutions, we further process the magnetograms by smoothing them, extrapolating mid-latitude data poleward, and removing any monopole components [e.g., *Riley et al.*, 2012].

We chose Carrington Rotation (CR) 2207 (09/02/2018 - 09/29/2018) for our analysis since it occurred during a time period that was: (1) relatively stable from one rotation to the next; (2) exhibited a simple solar minimum-like configuration with slow flow emanating from about the equator and large polar coronal holes producing fast, steady solar wind at higher latitudes; and (3) devoid of any significant CME activity. Figure 1 summarizes 12 realizations of ADAPT/GONG synchronic maps corresponding to the midpoint in time of CR 2207.

We note several points. First, overall, the realizations look very similar to one another. The two main clusters of active regions (at 80° and 240°) appear to be nearly identical, as does the overall structure of the polar regions. It is worth noting, however, that the fields have been visually saturated at ±10 G. Second, at smaller scales there are some subtle differences. For example, the structure of the polar regions, as evidenced by contours near ±10 G (the boundary between deep red/blue and white), changes from one realization to the next. In particular, the white excursions into the otherwise red/blue polar regions occur at slightly different longitudes from one panel to the next. Third, the shape of the active region (AR) fields, including the orientation of the bipoles, changes modestly from one realization to the next. Additionally, the strength of the AR fields is not the same. For example, consider the negative flux region south of, but between the two major ARs at $\sim$ 240° longitude. This is much weaker in realization 11 than in realization 12. These are, however, minor differences, and it is not clear based only on these maps what impact, if any, they may have on the evolution of CMEs in the solar wind. Only by simulating an ICME through all solutions can we assess their impact on the ToA of the ICME. It is, however, worth underscoring that these ADAPT realizations are just that: synchronic maps that are all consistent with the available observations. Thus, we cannot – a priori – say that one is better than another, and so they provide a useful way to capture (or, at least, provide a lower limit to) uncertainties due to the ambient boundary conditions.

2.2 Models

2.2.1 Ambient Solar Wind

Our goal in this study is not to attempt to find the best match between models of ICMEs and their observed signatures, but, for a range of typical values, to assess how sensitive the ToA of the event at Earth is to the various input parameters used to launch the CME. For this reason, it is not necessary to run the most sophisticated numerical model. In fact, since the goal is to generate a large number of solutions to estimate uncertainties, we chose an empirical background model to generate the ambient solar wind [*Riley et al.*, 2001; *Riley et al.*, 2012]. In this approach, the magnetic field of the corona is computed using the observed photospheric field maps shown in Figure 1, and the structure of the field is used to generate the boundary conditions for the heliospheric simulation. In partic-

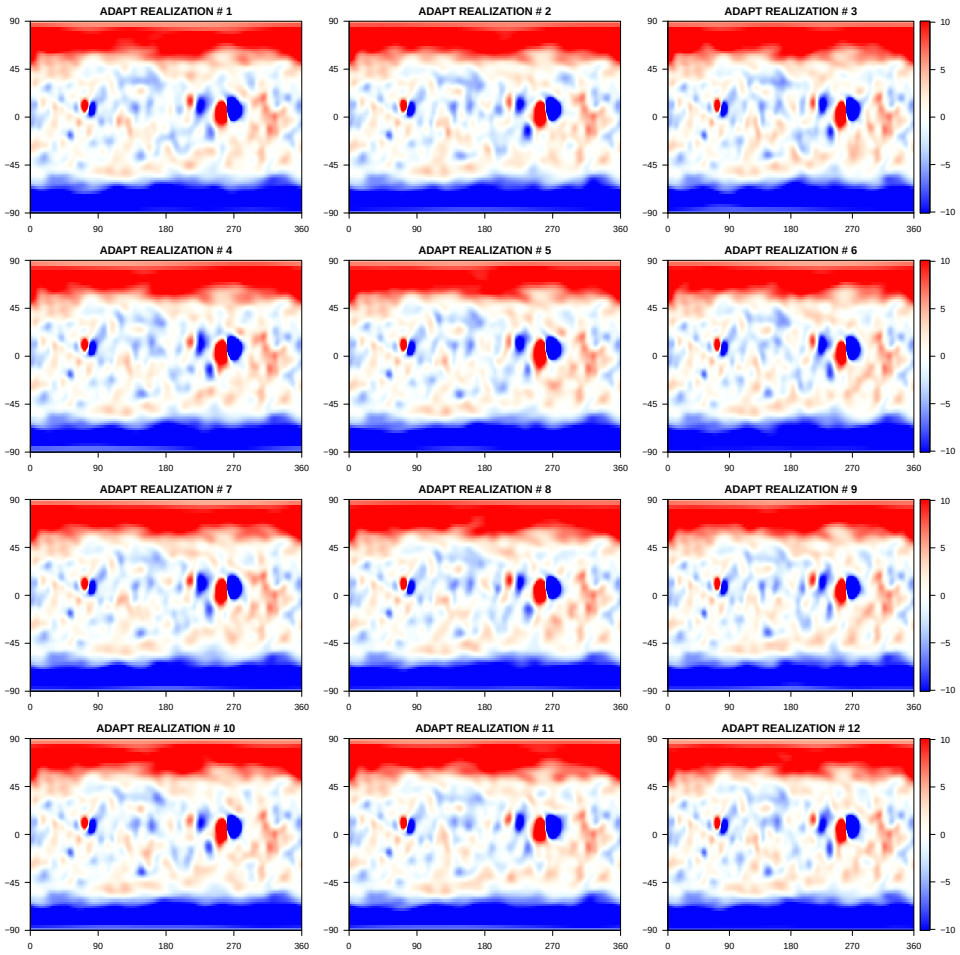

Figure 1. Twelve ADAPT Quasi-synchronic maps for Carrington rotation 2207. The panels have been saturated at ±10 G.

ular, we use the âĂIJDistance from the Coronal HoleâĂİ (DCHB) technique [*Riley et al.*, 2001] to generate longitude-latitude maps of solar wind speed at the inner boundary of the heliospheric calculation (at $30R_S$). The Radial component of the magnetic field is used directly from the coronal solution, and the other (normal) components of the field and velocity are set to zero. Pressure balance and momentum flux balance across the sphere at $30R_S$ are used to specify the remaining magnetofluid parameters, temperature and density, respectively. This approach is similar in concept to that employed by WSA+ENLIL [*Pizzo et al.*, 2015], except that WSA+ENLIL use expansion factor to specify the values of solar wind speed at the inner radial boundary of the heliospheric model. Although we have demonstrated that the DCHB method is generally more accurate than the WSA approach [*Riley et al.*, 2015], for the purposes of this investigation, either approach could be justified.

Figure 2 shows the computed radial speed at the inner boundary of the heliospheric calculation for the synchronic maps shown in Figure 1. We can make the same general comments about the overall similarity between each of the panels, but again, note the appearance of more subtle smaller-scale differences. In fact, these differences are more noticeable in the boundary conditions for solar wind speed than they were for the photospheric magnetic field, with the longitudinal alignment of fast-slow (or slow-fast) boundaries shifting by 5−10° in some cases. Additionally, the relative orientation (in the latitude-

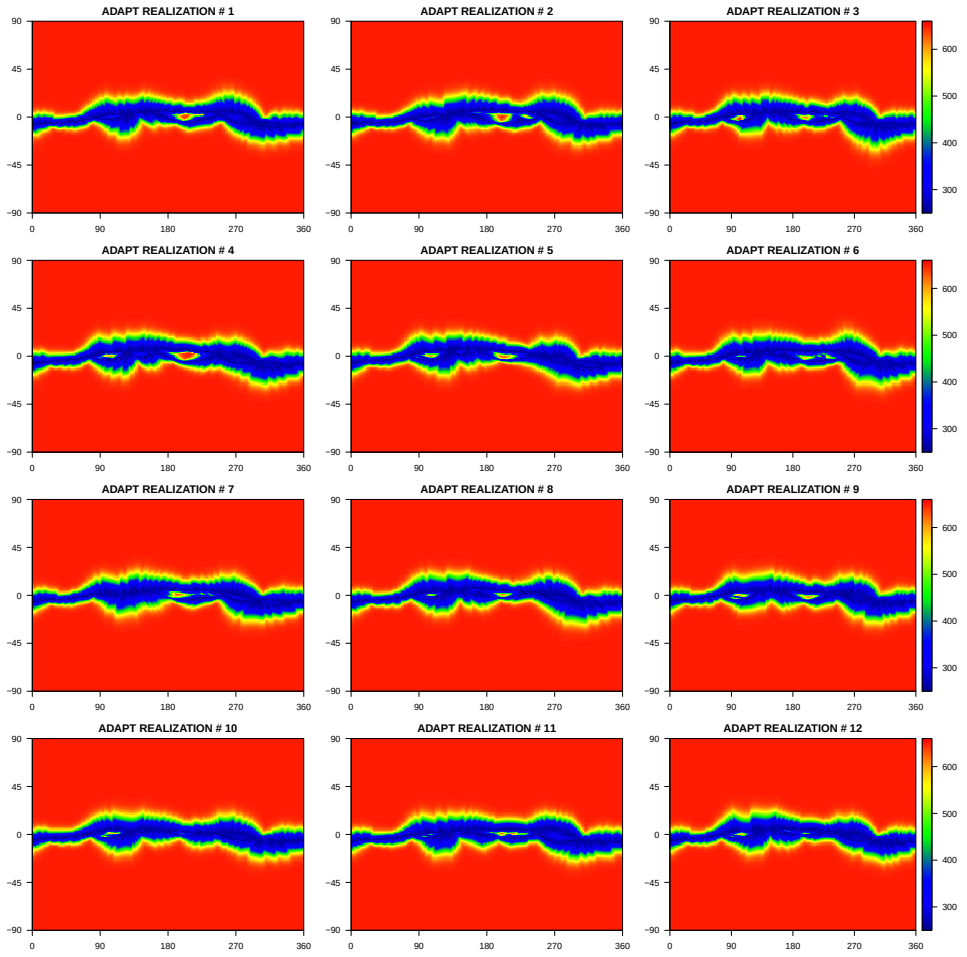

Figure 2. Computed radial speed at the inner boundary of the heliospheric model for Carrington rotation 2207.

longitude plane) of the fast-slow boundaries changes from one realization to the next. Although it is possible to infer how these differences will evolve (at least qualitatively) as the plasma propagates away from the Sun, it is difficult, if not impossible to reliably deduce how CME propagation (and deformation) will be affected by the differences.

2.2.2 CME Pulses

To mimic the launch of a CME from the upper corona, we follow the same prescription as other forecasting teams, by specifying the location, direction, speed, temperature, and density (or mass) of the ejecta as it passes through the inner radial boundary of the simulation. For the purposes of brevity, we report here on the following permutations: (1) Speed âĂŞ 800, 1000, and 1200 km s^{-1}; (2) Density âĂŞ ×1, ×2, and ×4 enhancement over a background base density of 500 cm^{-3}; and (3) Propagation direction/location âĂŞ 100 radial traces within a 15° circle about the CMEâĂŹs launch center. The temperature was assumed to be that of the ambient slow solar wind and the direction of propagation was assumed to be radial. Taken together, these variations represent reasonable uncertainties in the initial properties of CMEs observed in white light. The CME pulse is launched by smoothly raising the variableâĂŹs value over a one-hour interval, keeping it constant for the next 12 hours, and then smoothly returning it to ambient values over a one-hour

interval. Although the precise shape of the CME's profile can have a modest impact on the resulting structure of the ICME farther out in the solar wind [e.g., *Riley and Gosling*, 1998], it does not impact the analysis presented here.

With three inputs each for speed and density, 100 values for "location", and, for all of these combinations, 12 realizations of the ambient solar wind, there are a total of 10,800 plausible time series that could be observed at Earth. Again, we reiterate that, as a sensitivity study, there is no "ground truth" answer concerning which is the most correct, only different clusters of results to estimate the relative contribution to uncertainties due to our incomplete knowledge of the properties of the CME or the ambient solar wind into which it is propagating.

Regarding the "location" variable, rather than simulating 100 events with slightly different initial launch points in longitude and latitude (ϕ,λ), we took the more pragmatic approach of flying hypothetical spacecraft through different parts of the ejecta, within a $\pm 15^\circ$ cone of the CME center. Although strictly not the same, it effectively allows us to generate multiple realizations for uncertainties in the relative position of the ICME to the Earth. That is, rather than moving the ICME around, we are moving the EarthâĂŹs position around to generate appropriate realizations.

3 Results

We begin by assessing the impact of the background solar wind on ToA uncertainty. For each of the 12 realizations summarized in Figures 1 and 2, we launched an ICME with a speed of 1200 km s^{-1} and a density twice that of the base value. Figure 3 shows the resulting profiles measured at a hypothetical spacecraft located at $r = 1$ AU, $\lambda = 0^\circ$, $\phi = 180^\circ$, that is, at the center of origin of the ICME. Several points are worth making. First, ADAPT realizations have an important impact on the evolution of the ICME. Speed measurements differ significantly with a peak as low as 863 km s^{-1} to as high as 1026 km s^{-1}. This also affects the ToA of the leading edge of the CME disturbance, with the shock arriving over a window of more than twelve hours. Similar variations are seen in the other plasma and magnetic field parameters. The importance of this result cannot be overstated. Given that each of these realizations is equally valid, we cannot distinguish between the quality of the forecasts from each one. Thus, we infer that there is an intrinsic limitation of ± 7 hours (the time separating the arrival of the first and last realization at a point one-third of the way up the shock front) based only on our uncertainty in the magnetograms. Moreover, this assumes that the magnetograms represent some kind of "ground truth". In reality, we know that there are substantially larger differences between synoptic maps generated from different solar observatories [*Riley et al.*, 2014]. Thus, the true uncertainties from the choice of magnetograms is likely larger.

We can also analyze the arrival time of the ejecta more precisely by adding tracer particles into the simulation. That is, massless particles that are advected out with the solar wind. By placing them at the leading edge of the CME pulse, we can accurately track their arrival at 1 AU. Figure 4 summarizes the properties of the solar wind at 1 AU, again in the equatorial plane. These are traces of the solar wind that started approximately two days preceding the arrival of CME at Earth. Focusing first on the radial velocity, the ambient solar wind derived from the 12 ADAPT realizations can differ by approximately 100 km s^{-1} at both high and low speeds. There are also substantial relative differences in both tangential components of the field. Although it is tempting to conclude that, given the large radial velocity of the CME, these velocities probably do not contribute significantly to differences in arrival time, in fact they do. The dashed lines indicate the ToA for each of the CMEs within each realization, leading to $\sim \pm 2$ hours uncertainty in ToA. Note, however, that the CME arrival times associated with the highest solar wind speed just ahead of them are not always those that arrive first. This is probably related to the fact that when tracking these tracer particles, they are not traveling out radially, but also re-

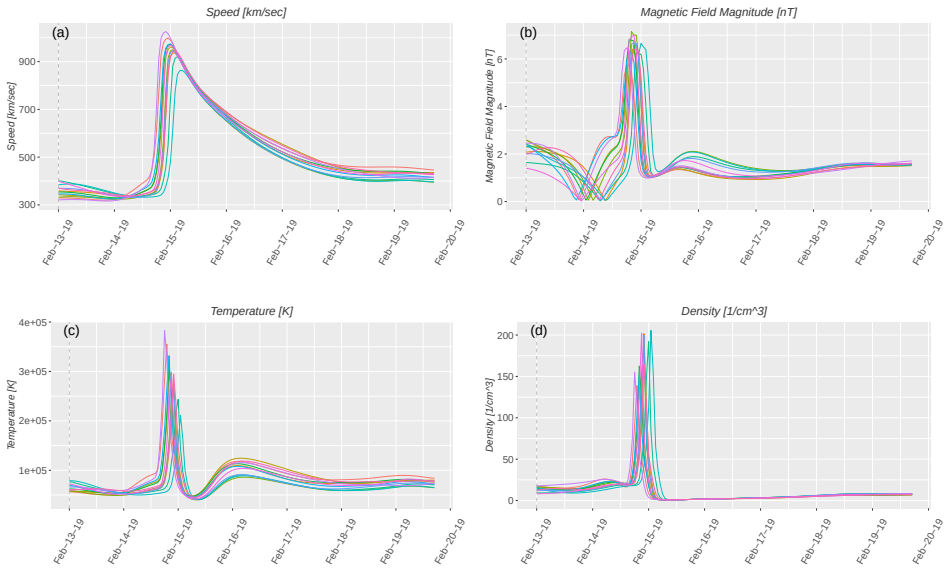

Figure 3. Solar wind profiles for a hypothetical CME launched into the solar wind conditions summarized in Figure 2. The CME had an initial speed of 1200 km s^{-1} and a density twice that of the base value. The dashed line marks the time that the CME was launched from the inner boundary.

sponding to shearing flows that move them in the transverse direction. Finally, it is worth noting that the uncertainty in ToA computed for the tracer particles (±2 hours) is notably smaller than those estimated from the time of arrival of the CME shock (±7 hours). In the former case, we are estimating ToA based on the time history of the particle as it advects through the solar wind, while in the latter, we are identifying the ToA from the passage of a shock (or steepened wave) across the observerâĂŹs position. Given the non-radial flow, it is possible that this plasma is laterally separated significantly from the parcel of plasma that launched at the CMEâĂŹs leading-edge center.

A final point worth making about the profiles in Figure 4 is that, despite the large variations upstream of the ICME from different realizations, none of the plasma shown from February 13 through to early February 15 have any impact upon the ToA of the ICME disturbance nor the deformation of its large-scale structure. Only the plasma directly ahead of the CME can interact with the CME pulse, and, by definition, this is limited to the region downstream of the fast-mode forward shock. Thus, while it is crucial to estimate the properties of the ambient solar wind near to, or surrounding the CME structure, the details of the solar wind away from this region matter little from a forecasting perspective. Of course, currently, there is no way to disentangle the two: large-scale models require global, or near global geometries. Moreover, the properties of the ambient solar wind in the ecliptic plane are modulated, to a large degree, by the properties of the polar magnetic field [*Riley et al.*, 2019] making it less likely that simpler 1-D or 2-D ad hoc approaches can accurately forecast the ambient solar wind into which the CME will be embedded and interact with.

Next, we estimate the impact of uncertainties in the ToA of CMEs based on errors in our estimation of the propagation direction of the CME. Even when multiple spacecraft observe the same event, it is unlikely that the true direction is known to within $5 - 15°$. As noted above, rather than running a suite of events where we launch an otherwise identical CME in slightly different directions, we can mimic the effect by following the loci of tracer particles within the CME that are spread out by a similar transverse amount,

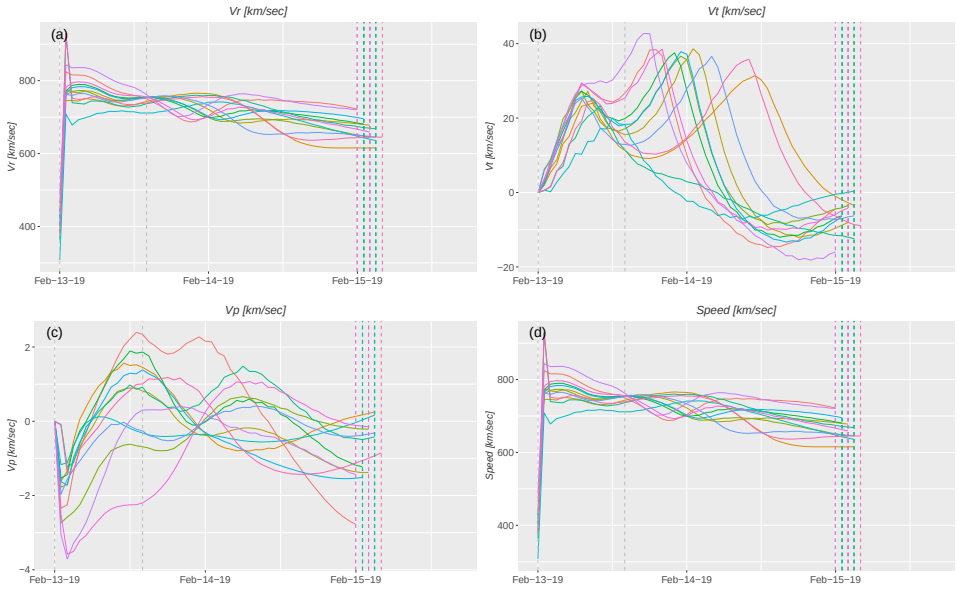

Figure 4. Upstream velocity components (in spherical coordinates: v_r, v_θ,v_ϕ) for the ambient solar wind realizations shown in Figure 2. The arrival of the ICME propagating through these solutions is indicated by the dashed vertical lines.

as shown in Figure 5. The two distributions (blue and red) encapsulate the worst (±15°) and best (±5°) forecast predictions, respectively, based on either one set of coronal observations to constrain the CME, or multiple observations from more than one spacecraft. In the worst case, with only observations from, say, Earth, it is likely that the CME ToA could be forecast to be between 40 and 59 hours. Or, equivalently, ±9.5 hours (using 5/95% quantiles). This is similar to the uncertainties prevalent in current forecasts of the ToA of ICMEs [*Riley et al.*, 2018]. If the uncertainties in initial direction can be constrained to within ±5°, the associated errors in ToA are substantially reduced, say, between 44 and 58 hours, or 5/95% CI: ±7 hours. (For comparison, using mean values and standard deviations would lead to estimates of: 41/55 or ±7 hours and 50/58 or ±4 hours, respectively).

We also investigated how uncertainties in the ToA of ICMEs depended on the initial speed of the ICME, which is generally only known to within ±200 km s^{-1}, but again dependent on the number and quality of the observations used to derive that estimate. As summarized in Figure 6, we visually infer that for a CME traveling at 1200, 1000, and 800 km s^{-1}, the ToA of the first tracer particle was delayed by approximately 4 hours for each 200 km s^{-1} drop in initial speed. More quantitatively, we computed the mean, median, range, s.d. and 5/95% CIs for the point where the speed exceeded 500 km s^{-1} (i.e, on the early ascending portion of the shock front). As an example, the median ToA for the 800, 1000, and 1200 km s^{-1} ICME was 690, 390, and 210 minutes, respectively. From this, we can infer that the average uncertainty was 180 and 300 minutes between successive ICMEs, or in total, 8 hours. Thus, we conclude that (at least for this event) if the speed is known to only within ±200 km s^{-1}, the associated uncertainty in ToA is $\sim$ ±4 hours. Comparing the traces, we can make several remarks. First, prior to the arrival of the shock, all profiles are the same, that is, the only variability is due to the ADAPT realizations. Second, the compression region driven by the speed increase, and visible in the field magnitude, temperature, and density, is centered on the initial speed gradient and, thus, is staggered in time in relation to the phasing of the shock location. Third, the amplitude of the compression is in proportion to the jump in speed, although the fractional

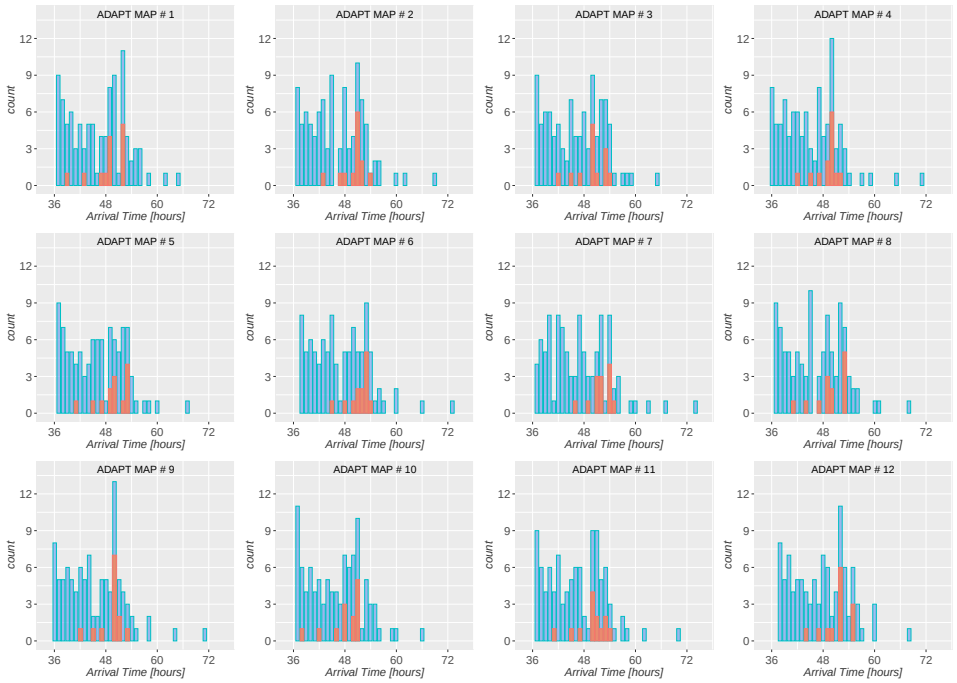

Figure 5. Histogram of arrival times for a set of tracer particles embedded at the leading edge of the cone-model CME. The larger (blue) group were all within ±15°of center, while the smaller (red) group were all within ±5° of the center.

change above background values increases from one parameter to the next, with density showing a more than doubling between each of the velocity pulses. Fourth, the rarefaction created on the declining speed profile is proportionately longer for the faster ICME, but the trailing edge of this wave merges into the background flow at roughly the same time for each case. Fifth, the spread in the ToA of the shock front due to (1) the different realizations (clusters of profiles of the same colors) and (2) the different initial speed jumps (sequential profiles of different colors) are of approximately the same magnitude, suggesting that these sources of uncertainty are roughly comparable.

Finally, it is well appreciated that the mass of the CME is one of the most difficult properties to determine with any degree of accuracy [e.g., *Vourlidas et al.*, 2010]. To explore what kind of impact this might have, we considered the effects of doubling (or halving) the initial mass within the ejecta. Using the same analysis as described above for uncertainties in CME speed, we found that the difference for mass uncertainties was more modest; $\sim$ ±2.5 hours separated each ICME profile for a given ambient solar wind realization (Figure 7). Visually, given the fact that the profiles of different colors overlap much more, it is clear that the choice of ADAPT realization has a much larger impact on the ToA than the inferred mass of the CME. However, it is quite conceivable that mass uncertainties are larger than the factor of two assumed here. Unfortunately, even this uncertainty is âĂŸuncertain.âĂŹ In comparison with Figure 6, we also note that modifying the mass of the ICME does not generate the same variations in the structure of the events. That is, ICMEs of the same speed, differing only in mass, produce more dynamically similar events. More massive events arrive sooner, have a modestly higher peak speed, field strength, temperature, and density, but do not have unique features, such as the erosion in peak speed seen in the case of the 800 km s^{-1} event in Figure 6.

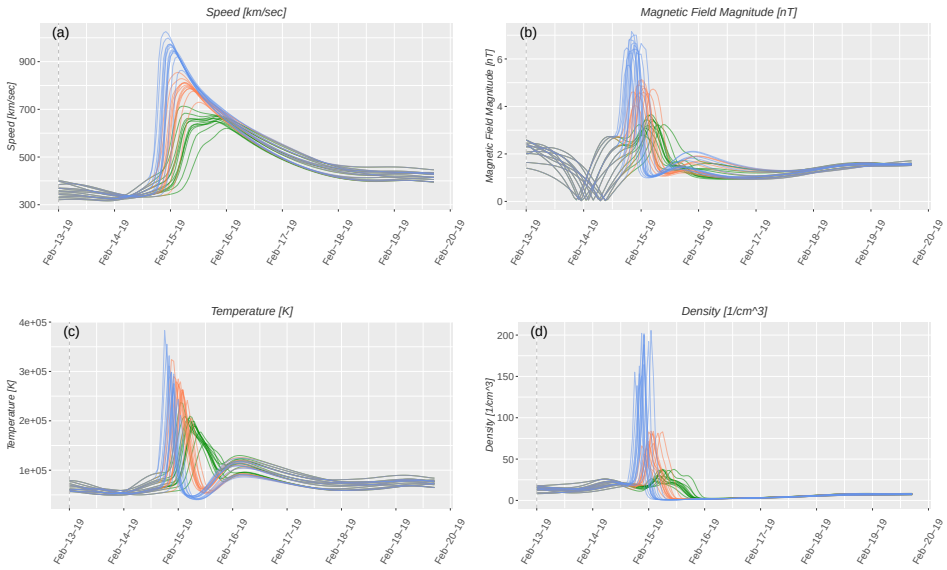

Figure 6. Comparison of arrival times for ICMEs with speeds 800 (green), 1000 (red), and 1200 (blue) km s^{-1}: (a) Speed; (b) magnetic field magnitude; (c) temperature; and (d) density.

4 Conclusions and Discussion

In this study, we have investigated the main sources of error in predicting a CME's ToA at Earth: (1) the initial properties of the ejecta, including its speed, mass, and direction of propagation; and (2) the properties of the ambient solar wind into which it propagates. To estimate the relative contribution to ToA errors, we constructed a set of numerical experiments of cone-model CMEs where we varied the initial speed, mass, and direction of the ejecta at the inner heliospheric boundary. Additionally, we built an ensemble of 12 ambient solar wind solutions using realizations from the Air Force's ADAPT model. We found that each point of uncertainty contributed between ±2.5 to ±7 hours of uncertainty to the estimate of the CME's ToA. Importantly, different realizations of the input magnetic synoptic maps resulted in errors of a similar magnitude, suggesting that estimates of ToA will continue to be plagued with intrinsic errors of $\sim$ ±10 hours until tighter constraints can be found for these boundary conditions, which will likely require more comprehensive observations of the Sun. Finally, our results suggest that there are clear benefits to focused investigations aimed at reducing the uncertainties in: CME speed, mass, direction, and input boundary magnetic fields.

Our results explain – to a large degree – the errors found in the forecasts made for the CCMC's "CME Arrival Time Scoreboard" [*Riley et al.*, 2018]. A combination of uncertainties in CME speed, direction, and mass, as well as uncertainties in the structure of the background solar wind into which the CME is propagating all appear to contribute to varying degrees. It is not surprising, therefore, that none of the models can make estimates where the MAE is smaller than about 12 hours. It is worth noting, however, that different models tend to focus on different aspects of the forecasting pipeline. Thus, it may be possible to combine the best practices from different techniques and improve skill scores, at least modestly.

Uncertainties in the properties of the ambient solar wind were shown to have a significant effect in the arrival time of the CME at Earth, in spite of the fact that our analysis was based on only modest differences between each of the 12 realizations calculated for

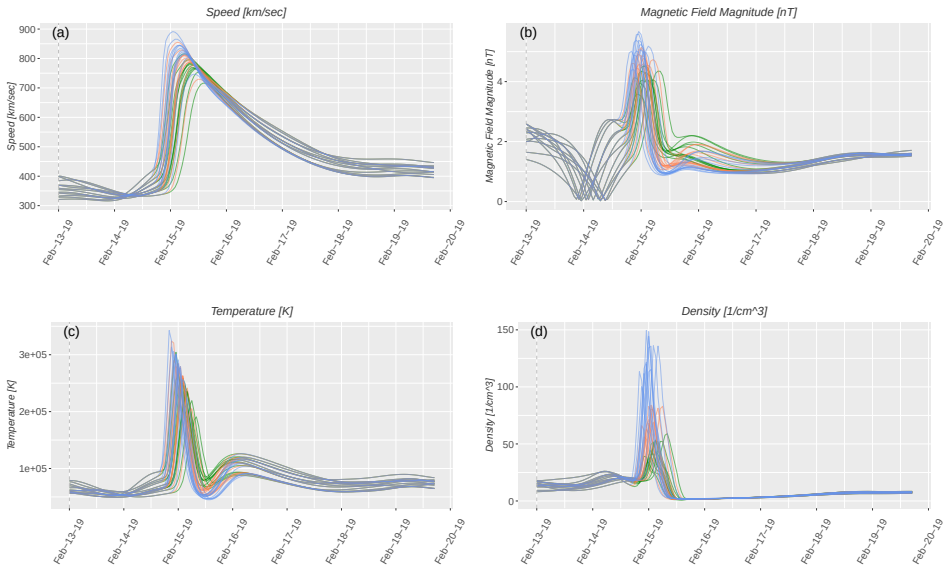

Figure 7. Comparison of arrival times for ICMEs density enhancements of ×1 (green), ×2 (red), and ×4 (blue) above background for, a 1000 km s^{-1} CME: (a) Speed; (b) magnetic field magnitude; (c) temperature; and (d) density.

one ADAPT map. As we have demonstrated previously [*Riley et al.*, 2014, 2012], forecasts using magnetogram data from different solar observatories will further increase the differences in the properties of the ambient solar wind, and hence, lead to even larger disparities in the arrival time of the ICME at Earth. These errors, can only be fully addressed by new, comprehensive observations of the Sun that, ideally, would cover 4π steradians of the solar surface. In practice, such a mission would require at least two polar orbiting spacecraft, together with at least three near-ecliptic spacecraft [*Riley et al.*, 2006]. In lieu of that, we suggest that modest gains may be obtained from improvements to the data assimilation procedure in the ADAPT map pipeline. A crucial aspect of this would be the extrapolation and "filling in" of missing polar observations, which are key for improving forecasts, even in the ecliptic plane [*Riley et al.*, 2019].

Uncertainties in CME speed, direction, and mass also resulted in significant errors in arrival time. Ultimately, we believe that first-principles models, which include the eruption of the CME and its propagation through the low corona, will produce the most accurate forecasts; however, in analogy with meteorological advances in the 1980âĂŹs and 1990âĂŹs, our understanding of the system has not matured to the point that these models can outperform empirical models. Thus, near-term advances will likely come from constraining the properties of the ejecta in the high corona. Analysis of multi-spacecraft white-light observations suggests that this approach can produce more accurate estimates of the initial properties of the CME than single-spacecraft observations, although this has not yet been demonstrated against global MHD simulations, for which there is an albeit idealized "ground truth".

Our results are broadly consistent with those of *Pizzo et al.* [2015], who found that different solutions produced deterministic (non-chaotic) estimates for ToA. Additionally, while we cannot quantitatively compare the dispersion in ToAs directly, the qualitative spread of their results is consistent with ours (compare their Figures 10, 11, 14, and 16 with our Figures 3 - 7). Our study also provides an independent assessment that the results of *Pizzo et al.* [2015] are insensitive to any specific aspects of the forecasting pro-

cess, including: (1) the particular numerical model being used; (2) the resolution of the simulations; (3) the empirical prescription of the ambient solar wind; (4) the choice of time period under study; and (5) the specification and values of the CME pulses. However, our results extend the *Pizzo et al.* [2015] study in several important ways. First, we drove the CMEs through realistic ambient backgrounds, modeled using realizations of the observed photospheric magnetic field. Second, we considered uncertainties in the CME pulse profiles that were based on the likely observation errors associated with estimating these parameters (speed, location, and mass) from white-light measurements. And third, we quantified the errors associated with each component in the modeling chain from the Sun to the Earth.

This study is not, however, without limitations or caveats. First, we relied on a global heliospheric MHD algorithm to compute the evolution of the ICME from near the Sun to 1 AU. While the accuracy of such codes has been tested and validated over the years, it is worth noting that these algorithms tend to be numerically diffusive and, as such, tend to dissipate small-scale fluctuations. This likely leads to structures that are more laminar than would be observed. In terms of the results presented here, this would reduce the differences in ToA. Thus, the model results probably underestimate the spread in ToA. Second, and as already noted, our choice of 12 ADAPT realizations also provides a lower limit on the uncertainty in the magnetograms used to drive the ambient solar wind. Both differences in the actual numerical values of the flux as well as how regions that are not well observed (limbs, far-side, and poles) are assembled would produce even greater variability in the maps driving the ambient solutions. Third, our prescription of the CME was limited to a simple hydrodynamic pulse. While this represents the current âĂIJstate-of-the-artâĂİ, observed CMEs clearly have a strong and significant magnetic structure embedded within them. Thus, once models are capable of reliably incorporating flux rope structures, this will result in an additional degree of uncertainty, dependent on how the properties of the flux rope can be constrained. Fourth, CMEs are often associated with precursor events [e.g., *Gopalswamy et al.*, 2001]. This is particularly true for fast, and hence more geoeffective events. These can either provide a means for sweeping out ambient solar wind structure ahead of the CME under consideration, or act as an obstacle that the following CME interacts with. In either case, this added complexity will also act to disperse the predicted ToAs, that is, it will increase the uncertainty in the forecasts.

In this study, by design, we did not study an observed event. We were not attempting to uncover the "correct" answer. Instead, our goal was to quantify the sources of uncertainty in the ToA of CMEs. Forecasting observed events is, ultimately, a more important objective. However, in the case of predicting observed events, care must be taken to avoid biasing the results by adjusting input parameters to more closely match the observations. True forecasts, such as those submitted to the CCMC's "CME Arrival Time Scoreboard" avoid this problem by requiring submissions prior to the arrival of the CME at 1 AU. On the other hand, hindcasts, or "retrospective forecasts" can potentially result in overly-optimistic results, since the analyst may (inadvertently) adjust input parameters to improve the forecast, in which case, the forecast is more of a curve fitting exercise than a demonstration of a promising technique. Nevertheless, when applied over a sufficiently large number of events, this could provide important information for constraining the free parameters of the model. The final test, however, remains to predict future events, such as through the CCMC portal, and this should be an objective for any ICME forecasting tool. In the interim, rigorous hindcast exercises could be conducted using the events catalogued at the CCMC portal, together with code made available to compare the new model's results with those that originally made the forecasts [*Riley et al.*, 2018].

In closing, based on the results presented here, we suggest that there are fundamental limitations to the accuracy that current CME forecasting tools can achieve. Modest advances can be made by more thorough analyses, including comprehensive efforts to 'hindcast' many ICME events and use robust statistical approaches to better constrain free pa-

rameters. However, ultimately, the greatest improvements will only come from a substantial investment in the form of multi-viewpoint observations of the photospheric magnetic field and white-light images of the corona.

Acknowledgments

The authors gratefully acknowledge support from NASA (80NSSC18K0100, NNX16AG86G, 80NSSC18K1129, 80NSSC18K0101, 80NSSC20K1285, 80NSSC18K1201, and NNN06AA01C), NOAA (NA18NWS4680081), and the U.S. Air Force (FA9550-15-C-0001).

All model results analyzed in this study are (or will soon be) available from the following repository: Riley and Ben-Nun (2021b). In the interim, they can be downloaded from `www.predsci.com~/pete/research/riley-ben-nun-2021a/`.

References

Arge, C. N., D. Odstrcil, V. J. Pizzo, and L. R. Mayer (2003), Improved Method for Specifying Solar Wind Speed Near the Sun, in *Solar Wind Ten*, *American Institute of Physics Conference Series*, vol. 679, edited by M. Velli, R. Bruno, F. Malara, and B. Bucci, pp. 190–193, doi:10.1063/1.1618574.

Arge, C. N., C. J. Henney, J. Koller, C. R. Compeau, S. Young, D. MacKenzie, A. Fay, and J. W. Harvey (2010), Air Force data assimilative photospheric flux transport (ADAPT) Model. In: Maksimovic, M., Issautier, K., Meyer-Vernet, N., Moncuquet, M., Pantellini, F. (eds.), *Twelfth International Solar Wind Conference, AIP Conf. Proc.*, *1216*, 343–346, doi:10.1063/1.3395870.

Forbes, T. G., and J. Lin (2000), What can we learn about reconnection from coronal mass ejections, *J. Atmos. Sol.-Terr. Phys.*, *62*, 1499–1507.

Gopalswamy, N., S. Yashiro, M. L. Kaiser, R. A. Howard, and J. L. Boueret (2001), Radio signatures of coronal mass ejection interaction: Coronal mass ejection cannibalism?, *Astrophys. J.*, *548*(1), L91–L94.

Gosling, J. T., S. J. Bame, D. J. McComas, and J. L. Phillips (1990), Coronal mass ejections and large geomagnetic storms, *Geophys. Res. Lett.*, *17*, 901.

Mays, M., A. Taktakishvili, A. Pulkkinen, P. MacNeice, L. Rastätter, D. Odstrcil, L. Jian, I. Richardson, J. LaSota, Y. Zheng, et al. (2015), Ensemble modeling of cmes using the wsa–enlil+ cone model, *Solar Physics*, *290*(6), 1775–1814.

Odstrcil, D., P. Riley, J. A. Linker, R. Lionello, Z. Mikic, and V. J. Pizzo (2003), 3-D simulations of ICMEs by coupled coronal and heliospheric models, in *ESA SP-535: Solar Variability as an Input to the Earth's Environment*, pp. 541–+.

Odstrcil, D., P. Riley, and X. P. Zhao (2004), Numerical simulation of the 12 May 1997 interplanetary CME event, *J. Geophys. Res.*, *109*, 2116–+, doi:10.1029/2003JA010135.

Pizzo, V., G. Millward, A. Parsons, D. Biesecker, S. Hill, and D. Odstrcil (2011), Wang-Sheeley-Arge-Enlil Cone Model Transitions to Operations, *Space Weather*, *9*, 03004, doi:10.1029/2011SW000663.

Pizzo, V., C. Koning, M. Cash, G. Millward, D. Biesecker, L. Puga, M. Codrescu, and D. Odstrcil (2015), Theoretical basis for operational ensemble forecasting of coronal mass ejections, *Space Weather*, *13*(10), 676–697.

Riley, P., and J. T. Gosling (1998), Do coronal mass ejections implode in the solar wind?, *Geophys. Res. Lett.*, *25*, 1529.

Riley, P., J. A. Linker, and Z. Mikić (2001), An empirically-driven global MHD model of the corona and inner heliosphere, *J. Geophys. Res.*, *106*, 15,889, doi:10.1029/2000JA000121.

Riley, P., J. A. Linker, Z. Mikić, D. Odstrcil, T. H. Zurbuchen, D. Lario, and R. P. Lepping (2003), Using an MHD simulation to interpret the global context of a coronal mass ejection observed by two spacecraft, *J. Geophys. Res.*, *108*, 1272.

Riley, P., J. A. Linker, Z. Mikic, and R. Lionello (2006), Maximizing the Scientific Return of the Sentinels Mission using Global MHD Models, *AGU Fall Meeting Abstracts*, pp. C4+.

Riley, P., J. A. Linker, R. Lionello, and Z. Mikic (2012), Corotating interaction regions during the recent solar minimum: The power and limitations of global MHD modeling, *J. Atmos. Solar-Terr. Phys.*, *83*, 1–10, doi:10.1016/j.jastp.2011.12.013.

Riley, P., M. Ben-Nun, J. A. Linker, Z. Mikic, L. Svalgaard, J. Harvey, L. Bertello, T. Hoeksema, Y. Liu, and R. Ulrich (2014), A Multi-Observatory Inter-Comparison of Line-of-Sight Synoptic Solar Magnetograms, *Sol. Phys.*, *289*, 769–792, doi:10.1007/s11207-013-0353-1.

Riley, P., J. A. Linker, and C. N. Arge (2015), On the role played by magnetic expansion factor in the prediction of solar wind speed, *Space Weather*, *13*(3), 154–169.

Riley, P., M. L. Mays, J. Andries, T. Amerstorfer, D. Biesecker, V. Delouille, M. Dumbović, X. Feng, E. Henley, J. A. Linker, et al. (2018), Forecasting the arrival time of coronal mass ejections: Analysis of the ccmc cme scoreboard, *Space Weather*, *16*(9), 1245–1260.

Riley, P., J. A. Linker, Z. Mikic, R. M. Caplan, C. Downs, and J.-L. Thumm (2019), Can an unobserved concentration of magnetic flux above the poles of the sun resolve the open flux problem?, *The Astrophysical Journal*, *884*(1), 18.

Török, T., C. Downs, J. A. Linker, R. Lionello, V. S. Titov, Z. Mikić, P. Riley, R. M. Caplan, and J. Wijaya (2018), Sun-to-earth mhd simulation of the 2000 july 14 âĂIJbastille dayâĂİ eruption, *The Astrophysical Journal*, *856*(1), 75.

Vourlidas, A., R. A. Howard, E. Esfandiari, S. Patsourakos, S. Yashiro, and G. Michalek (2010), Comprehensive analysis of coronal mass ejection mass and energy properties over a full solar cycle, *The Astrophysical Journal*, *722*(2), 1522.

Figure.

ADAPT REALIZATION # 1

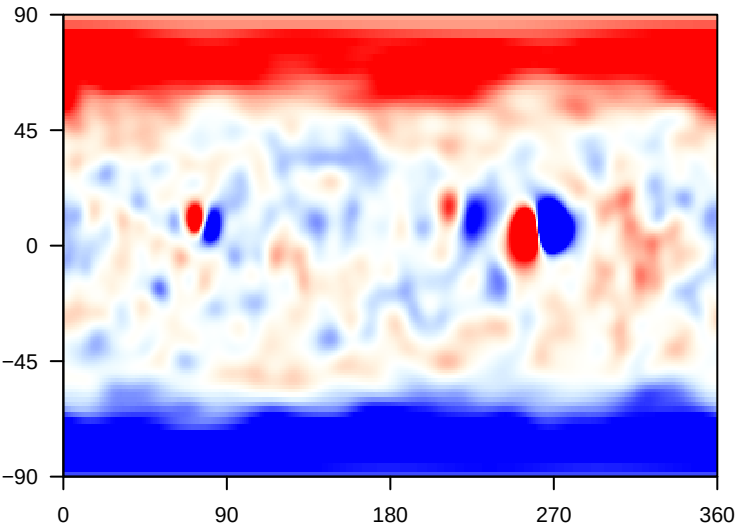

ADAPT REALIZATION # 2

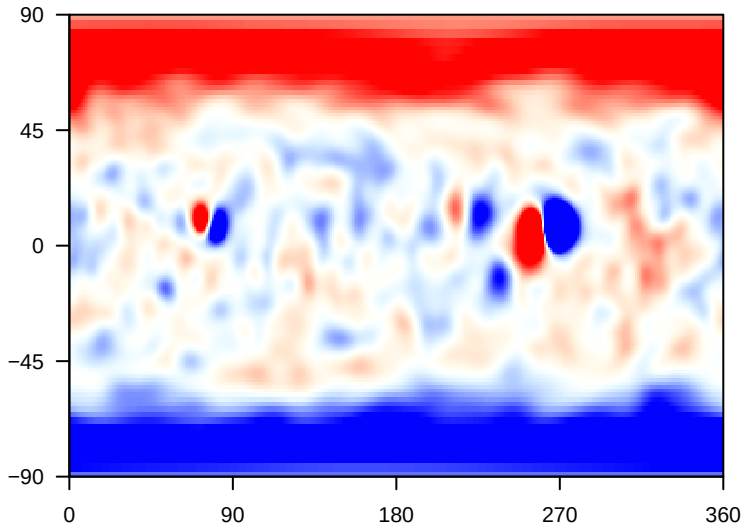

ADAPT REALIZATION # 3

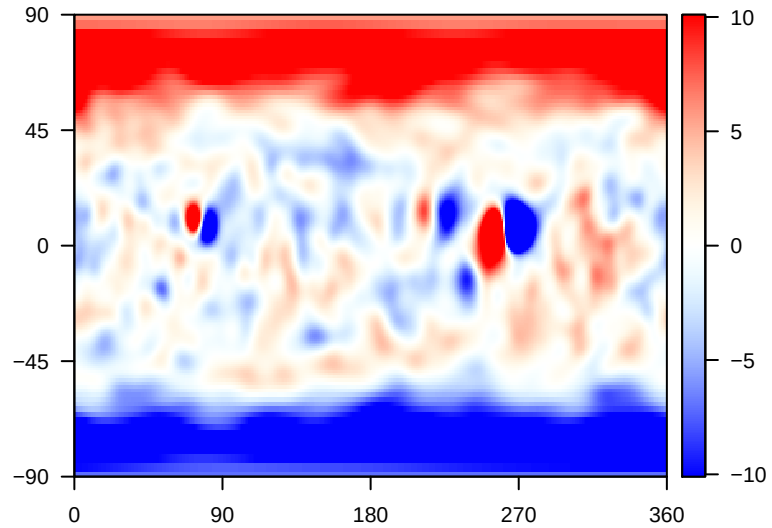

ADAPT REALIZATION # 4

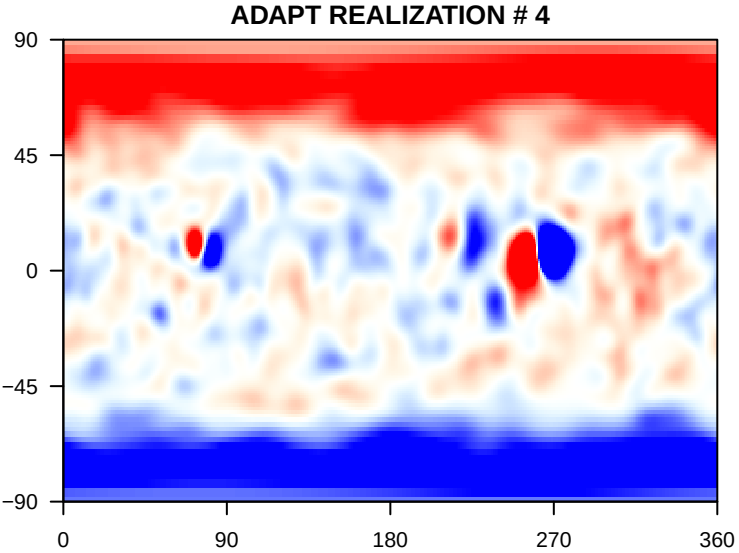

ADAPT REALIZATION # 5

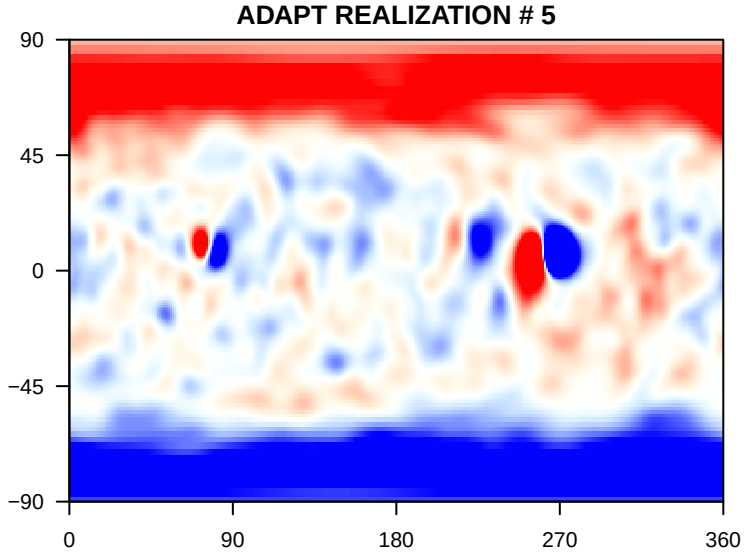

ADAPT REALIZATION # 6

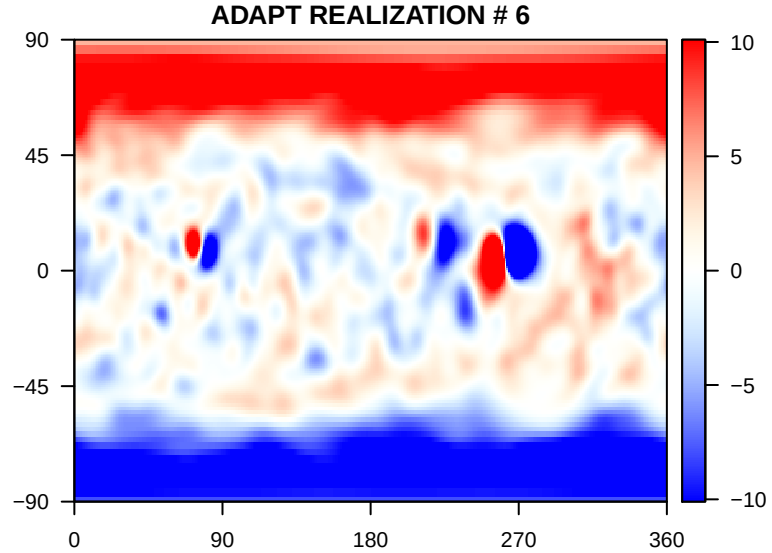

ADAPT REALIZATION # 7

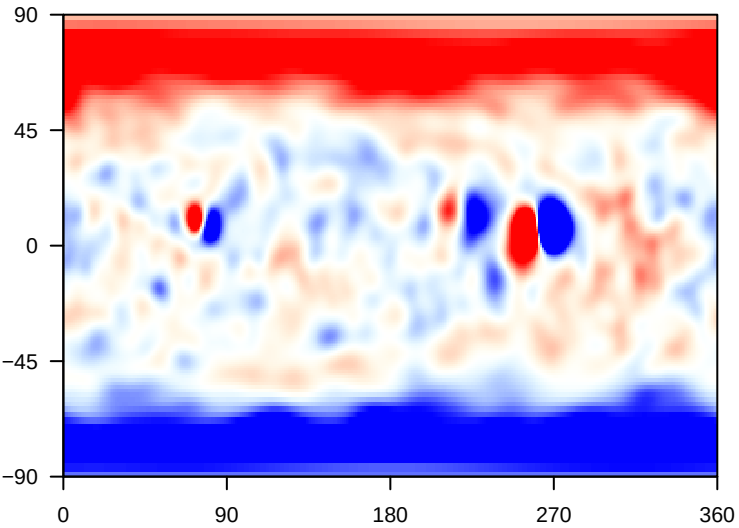

ADAPT REALIZATION # 8

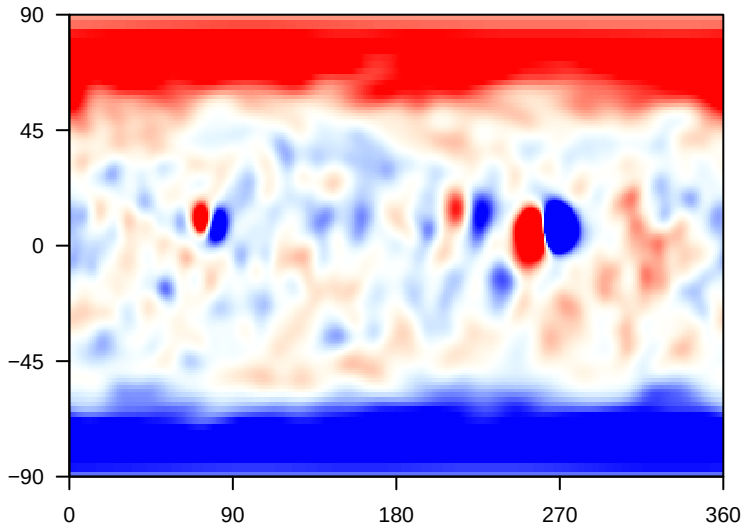

ADAPT REALIZATION # 9

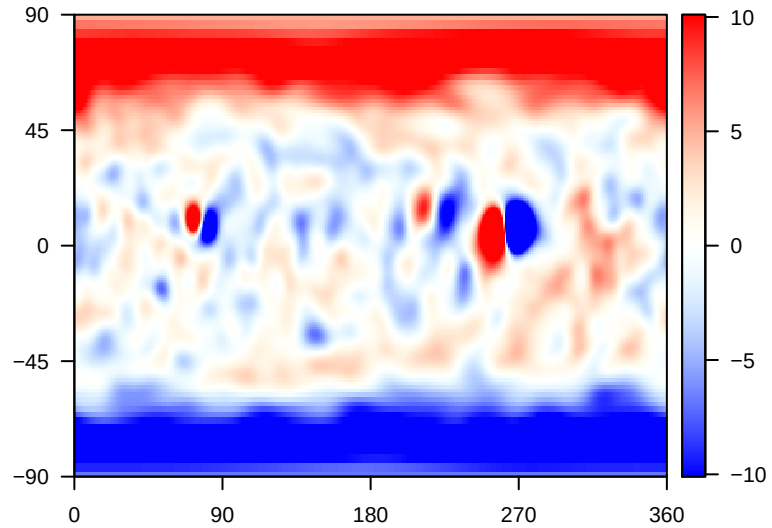

ADAPT REALIZATION # 10

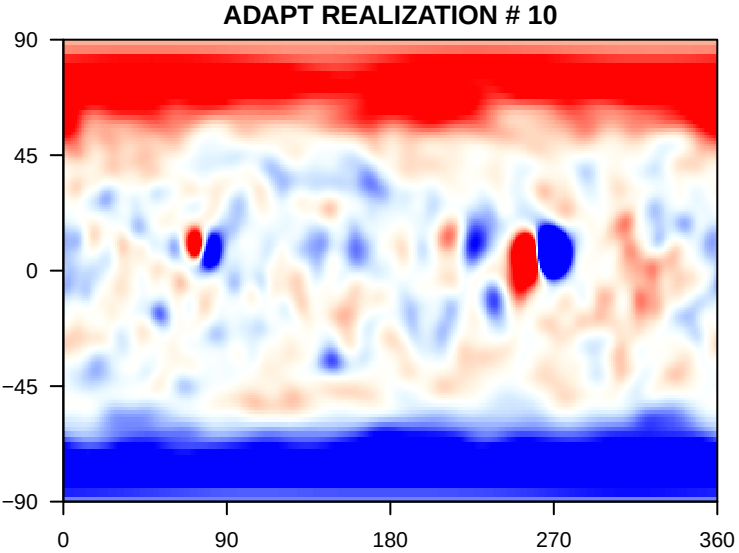

ADAPT REALIZATION # 11

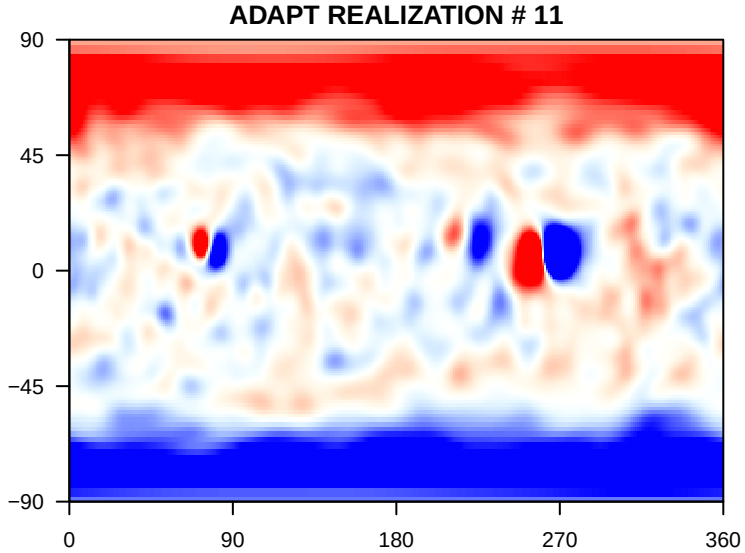

ADAPT REALIZATION # 12

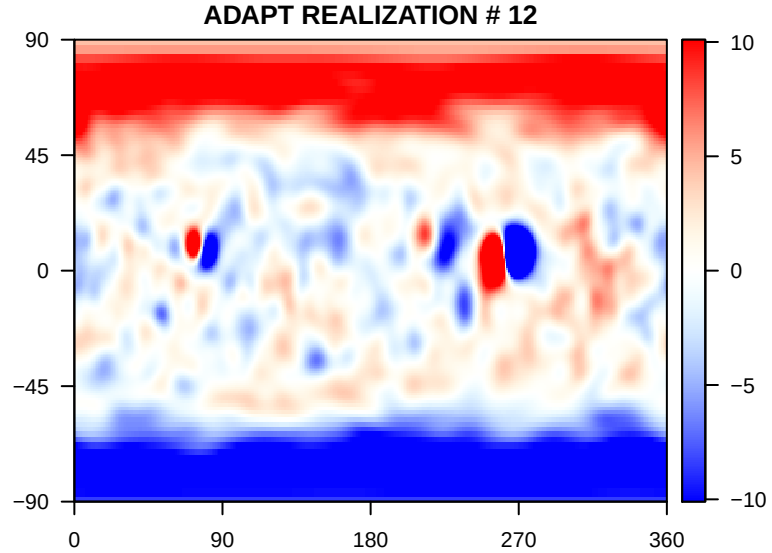

Figure.

ADAPT REALIZATION # 1

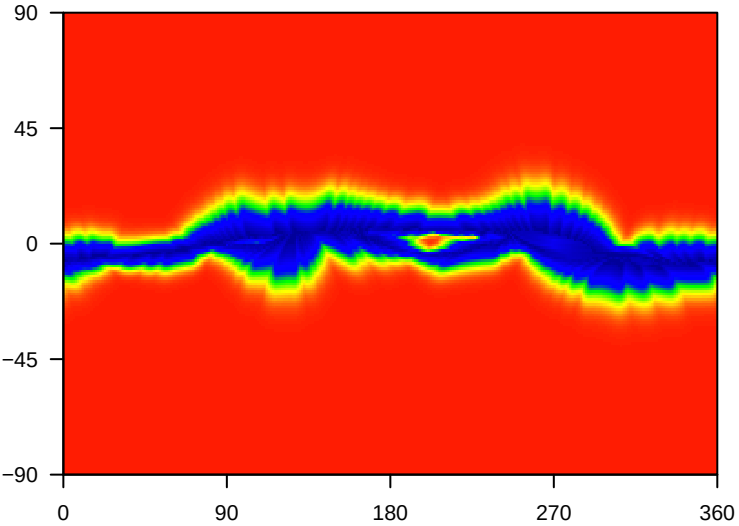

ADAPT REALIZATION # 2

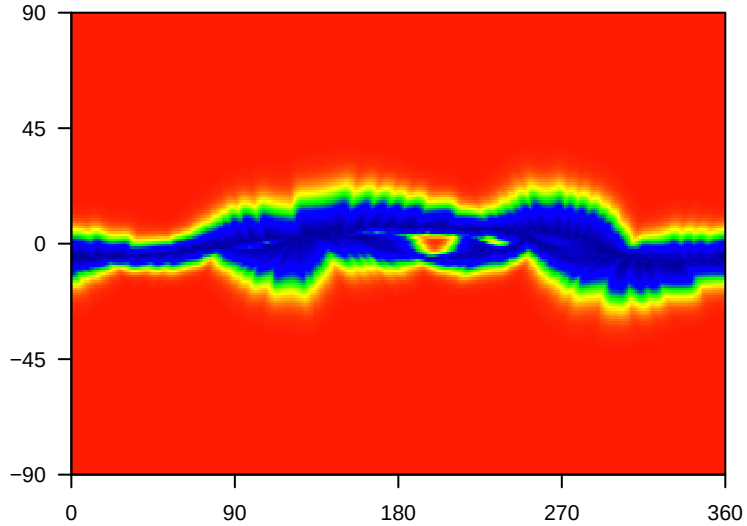

ADAPT REALIZATION # 3

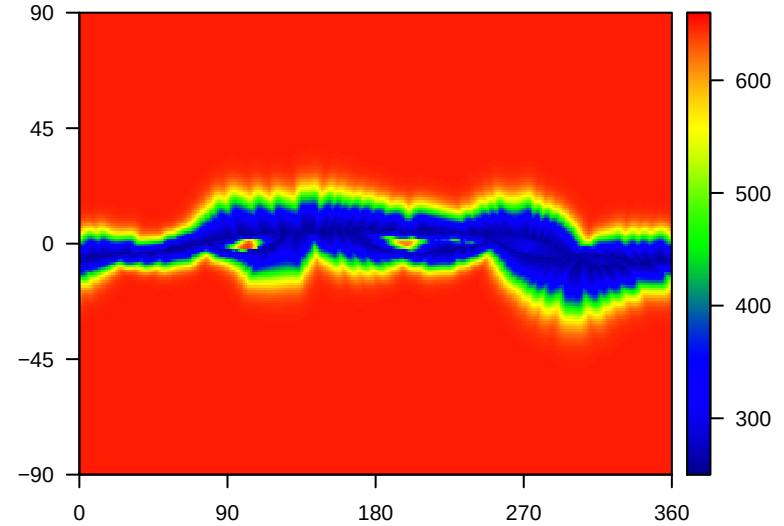

ADAPT REALIZATION # 4

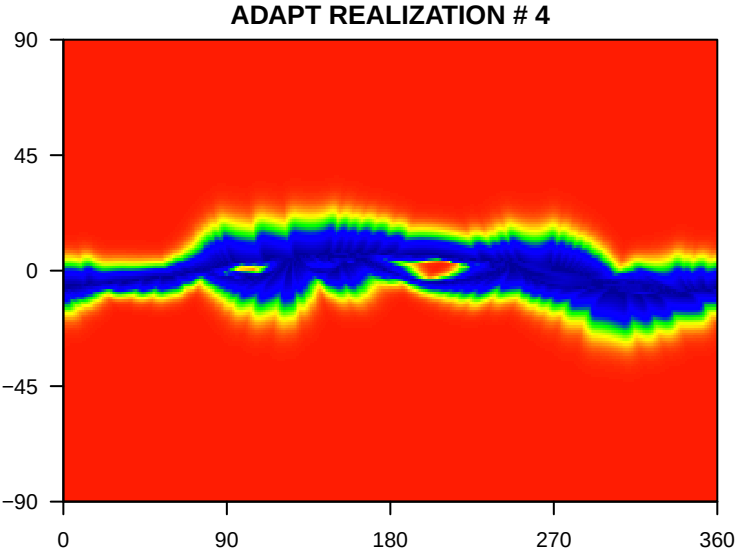

ADAPT REALIZATION # 5

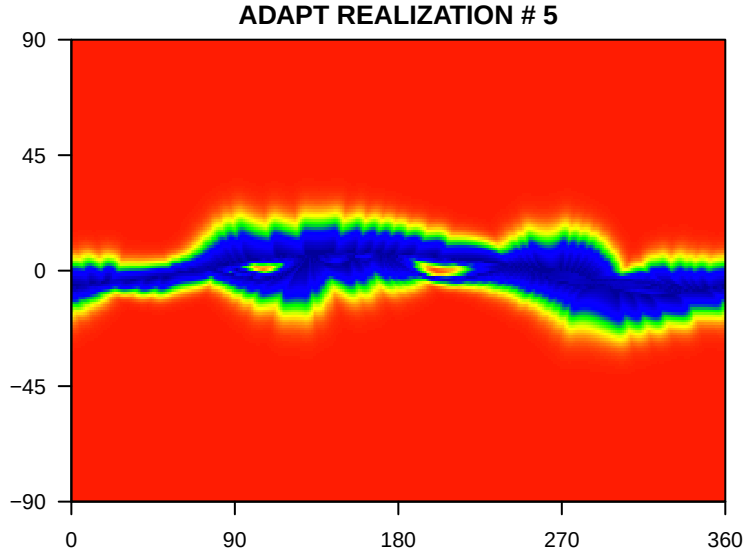

ADAPT REALIZATION # 6

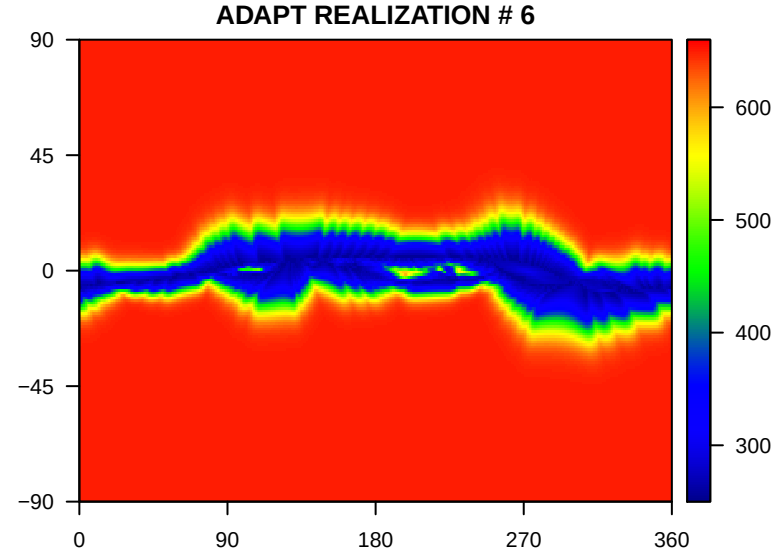

ADAPT REALIZATION # 7

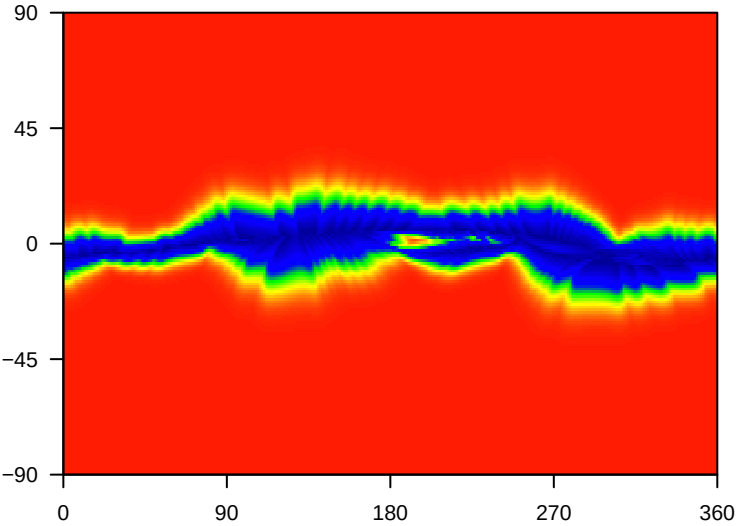

ADAPT REALIZATION # 8

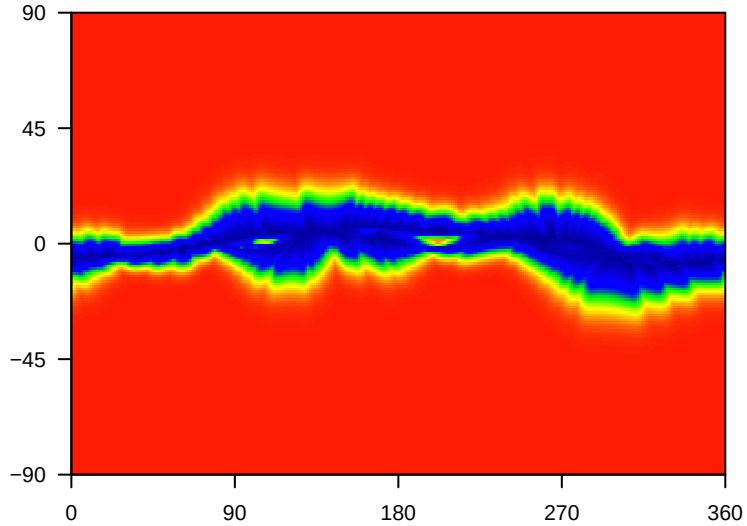

ADAPT REALIZATION # 9

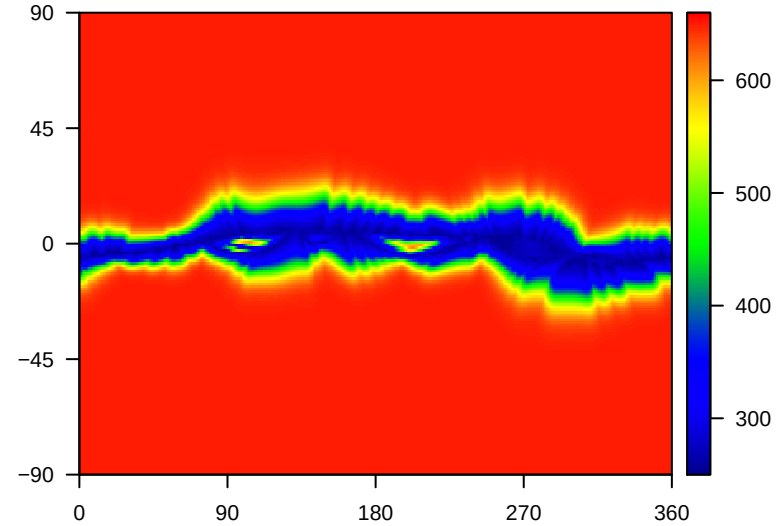

ADAPT REALIZATION # 10

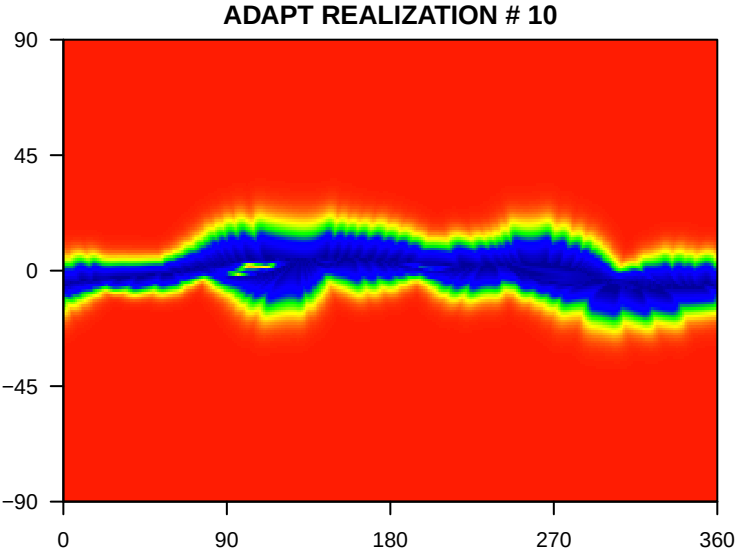

ADAPT REALIZATION # 11

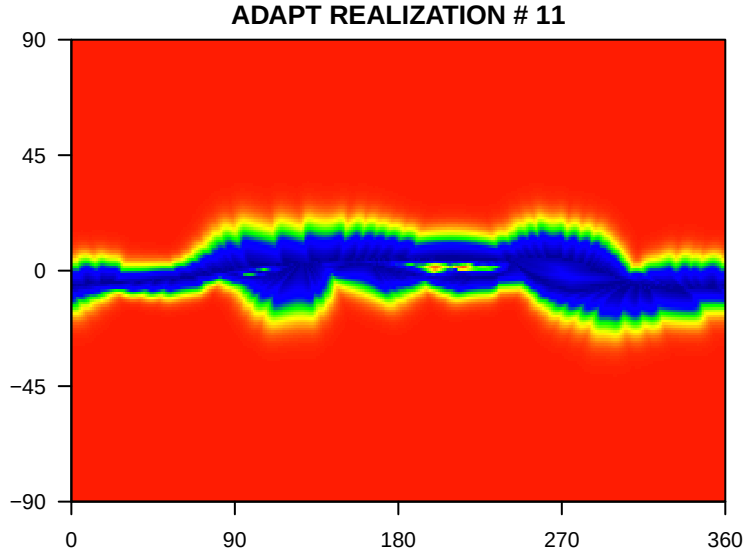

ADAPT REALIZATION # 12

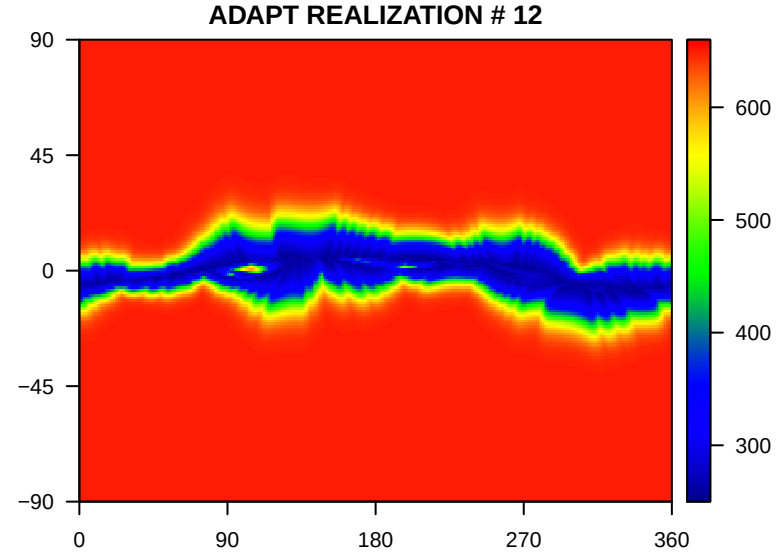

Figure.

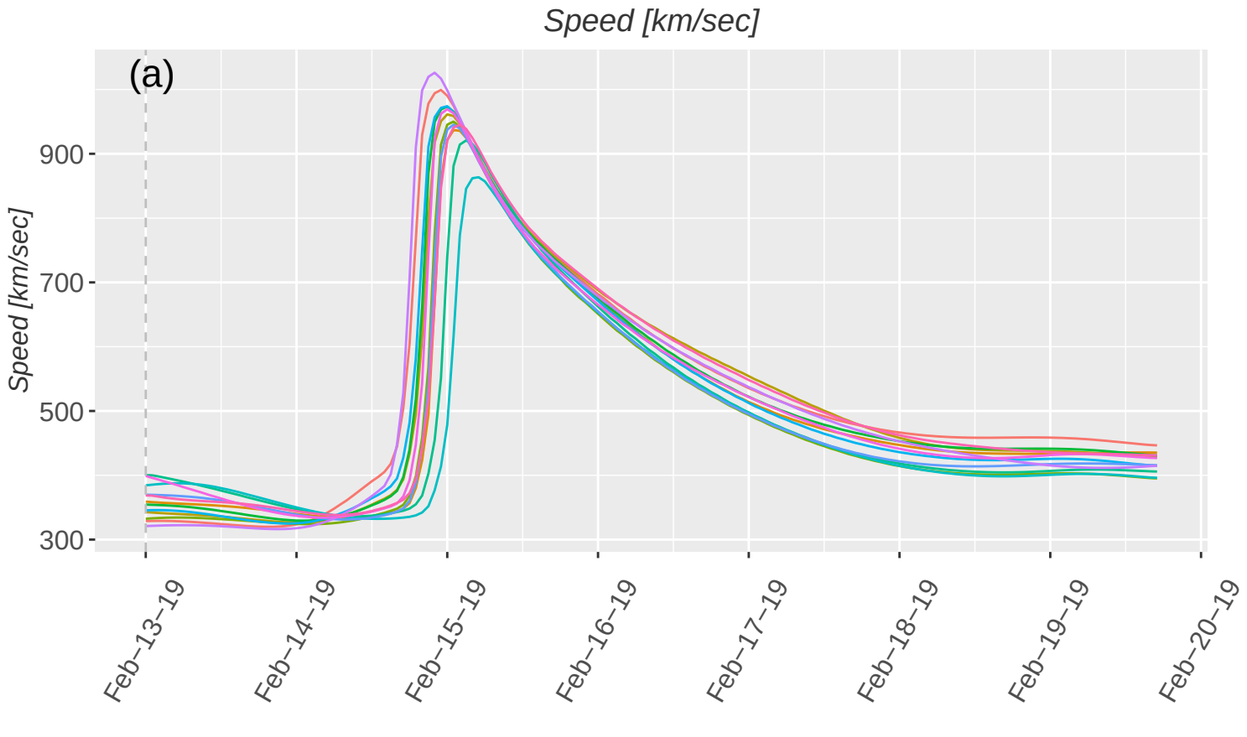
Speed [km/sec]
(a)
900
700
500
300
Speed [km/sec]
Feb–13–19
Feb–14–19
Feb–15–19
Feb–16–19
Feb–17–19
Feb–18–19
Feb–19–19
Feb–20–19

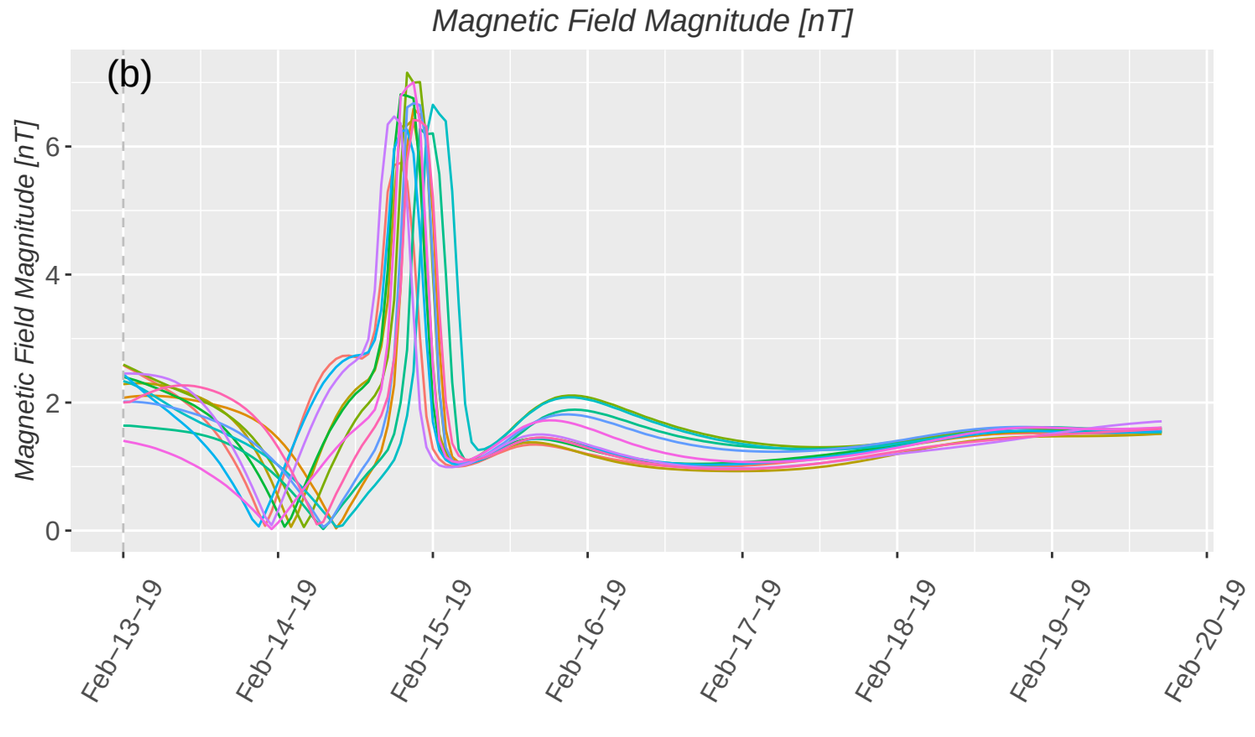
Magnetic Field Magnitude [nT]
(b)
6
4
2
0
Magnetic Field Magnitude [nT]
Feb–13–19
Feb–14–19
Feb–15–19
Feb–16–19
Feb–17–19
Feb–18–19
Feb–19–19
Feb–20–19

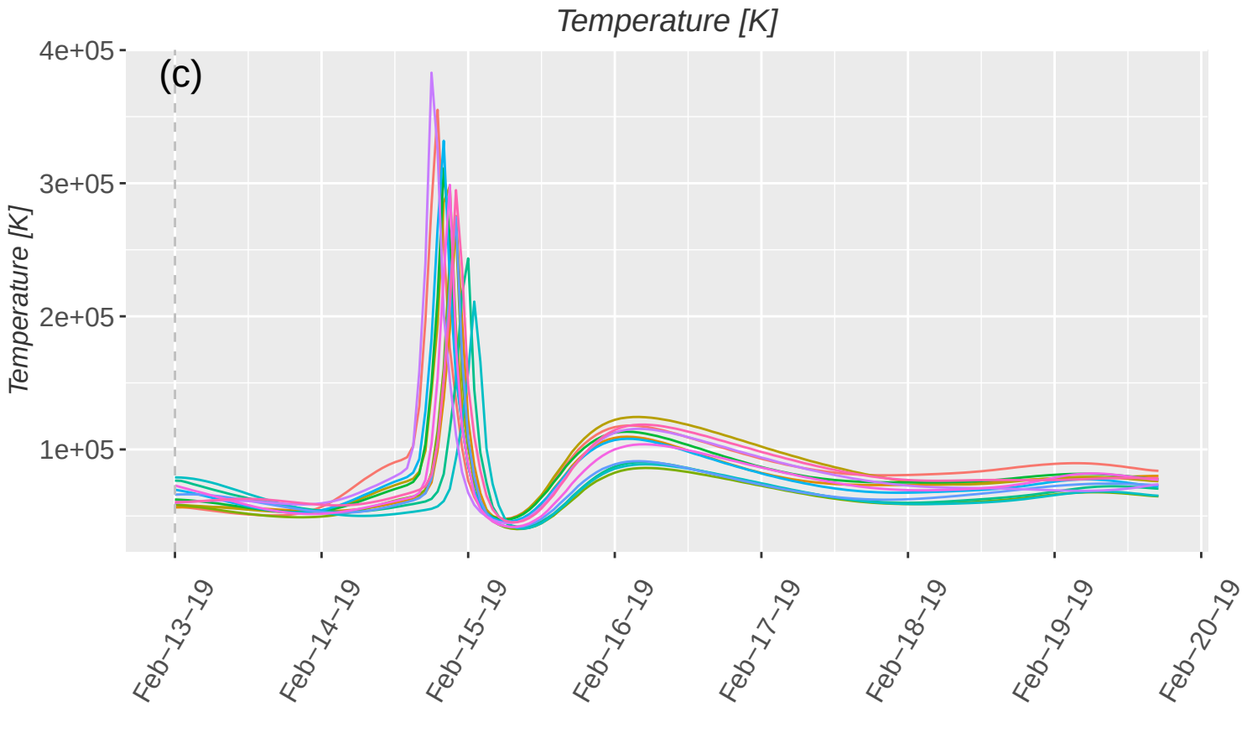
Temperature [K]
(c)
4e+05
3e+05
2e+05
1e+05
Temperature [K]
Feb–13–19
Feb–14–19
Feb–15–19
Feb–16–19
Feb–17–19
Feb–18–19
Feb–19–19
Feb–20–19

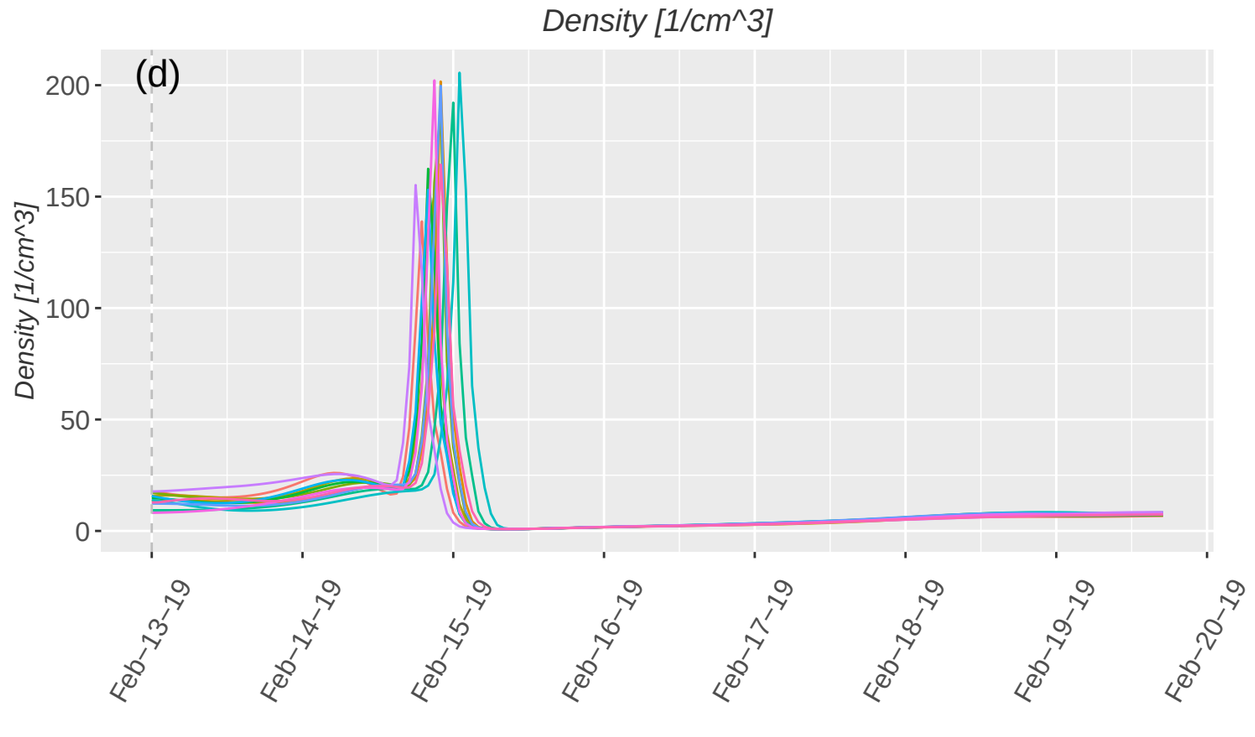
Density [1/cm^3]
(d)
200
150
100
50
0
Density [1/cm^3]
Feb–13–19
Feb–14–19
Feb–15–19
Feb–16–19
Feb–17–19
Feb–18–19
Feb–19–19
Feb–20–19

Figure.

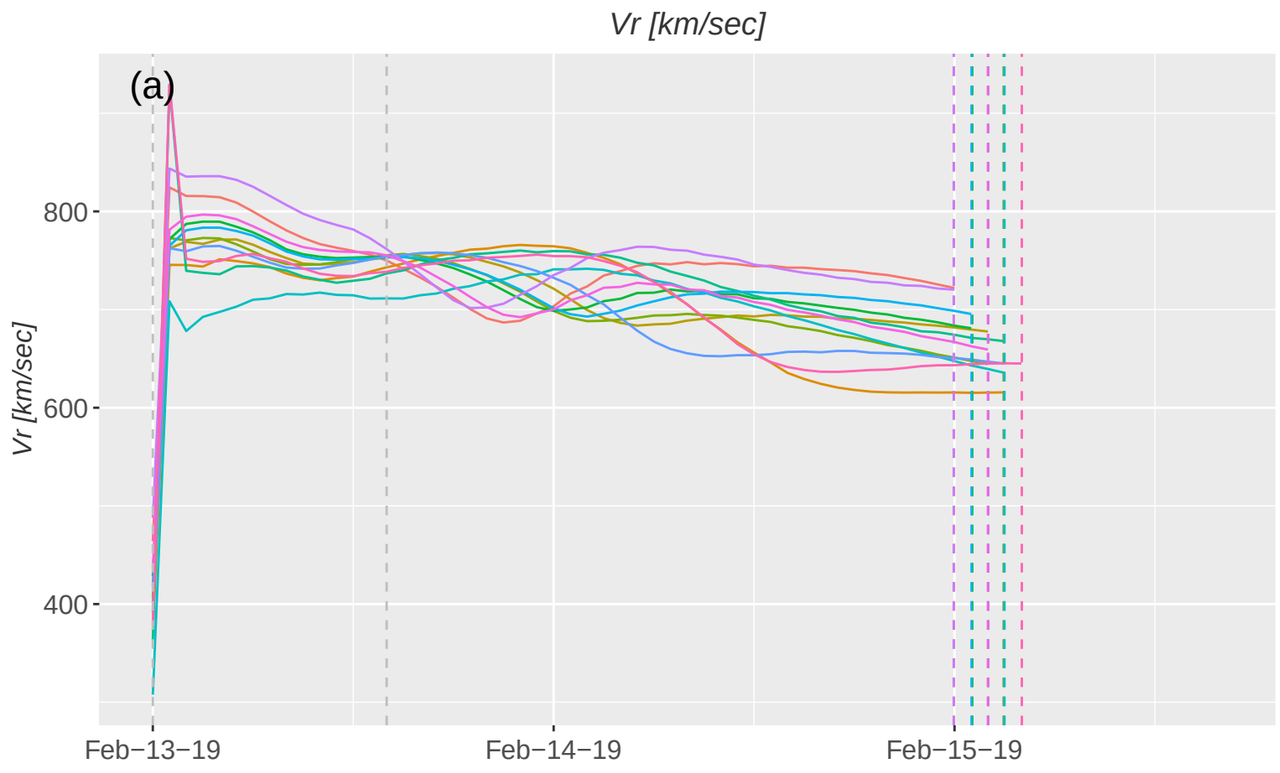
Vr [km/sec]
(a)
800
600
400
Vr [km/sec]
Feb−13−19
Feb−14−19
Feb−15−19

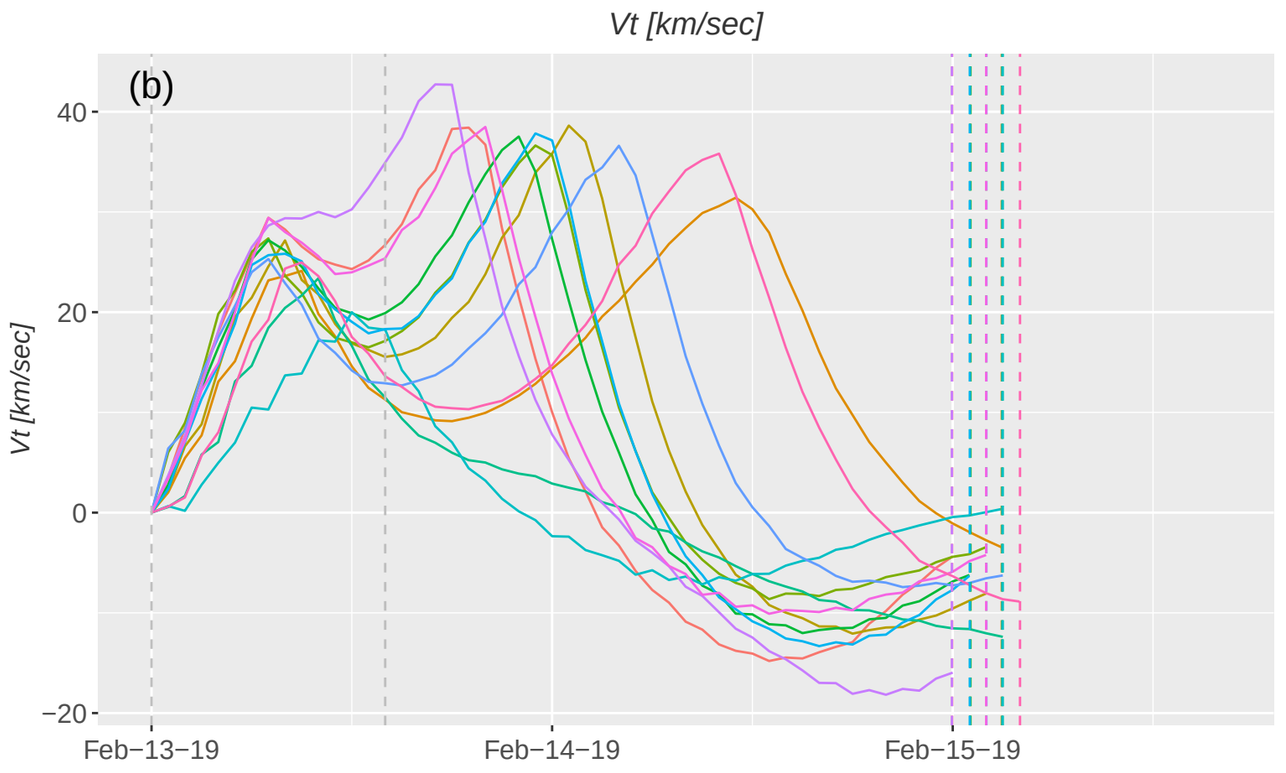
Vt [km/sec]
(b)
40
20
0
−20
Vt [km/sec]
Feb−13−19
Feb−14−19
Feb−15−19

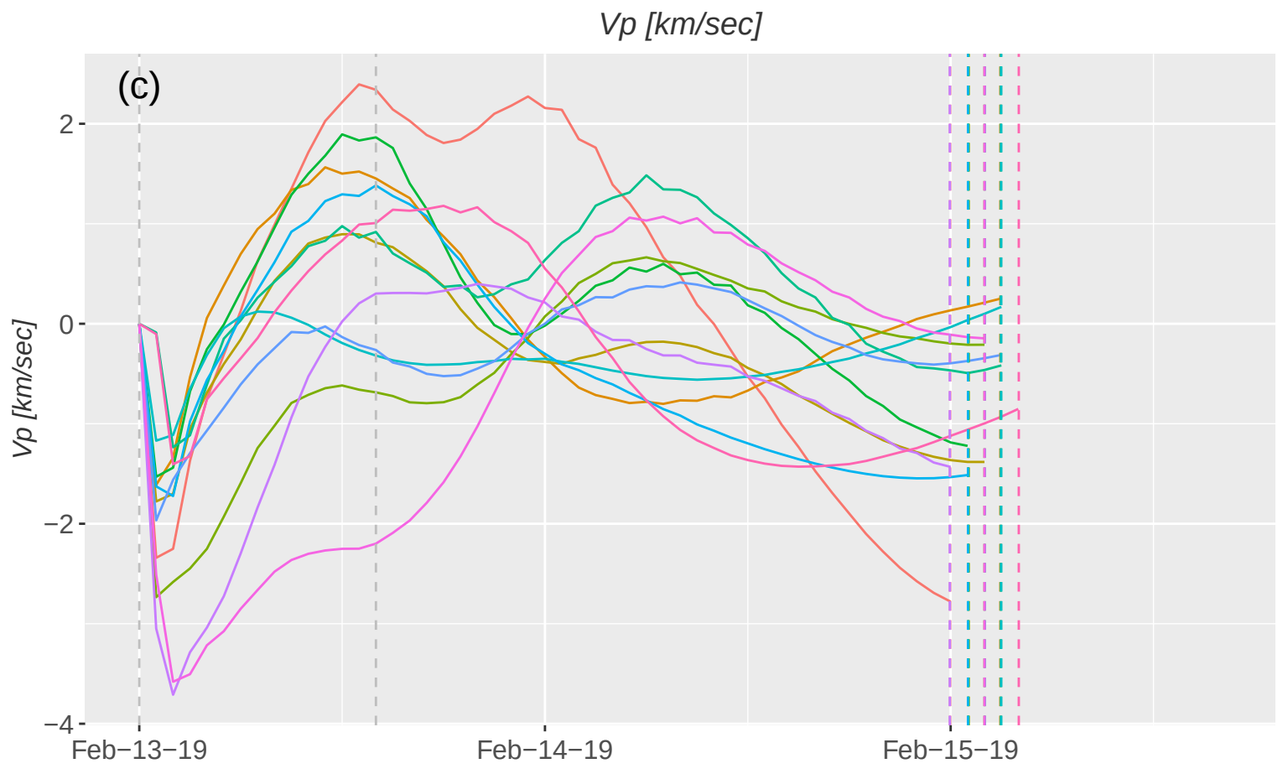
Vp [km/sec]
(c)
2
0
−2
−4
Vp [km/sec]
Feb−13−19
Feb−14−19
Feb−15−19

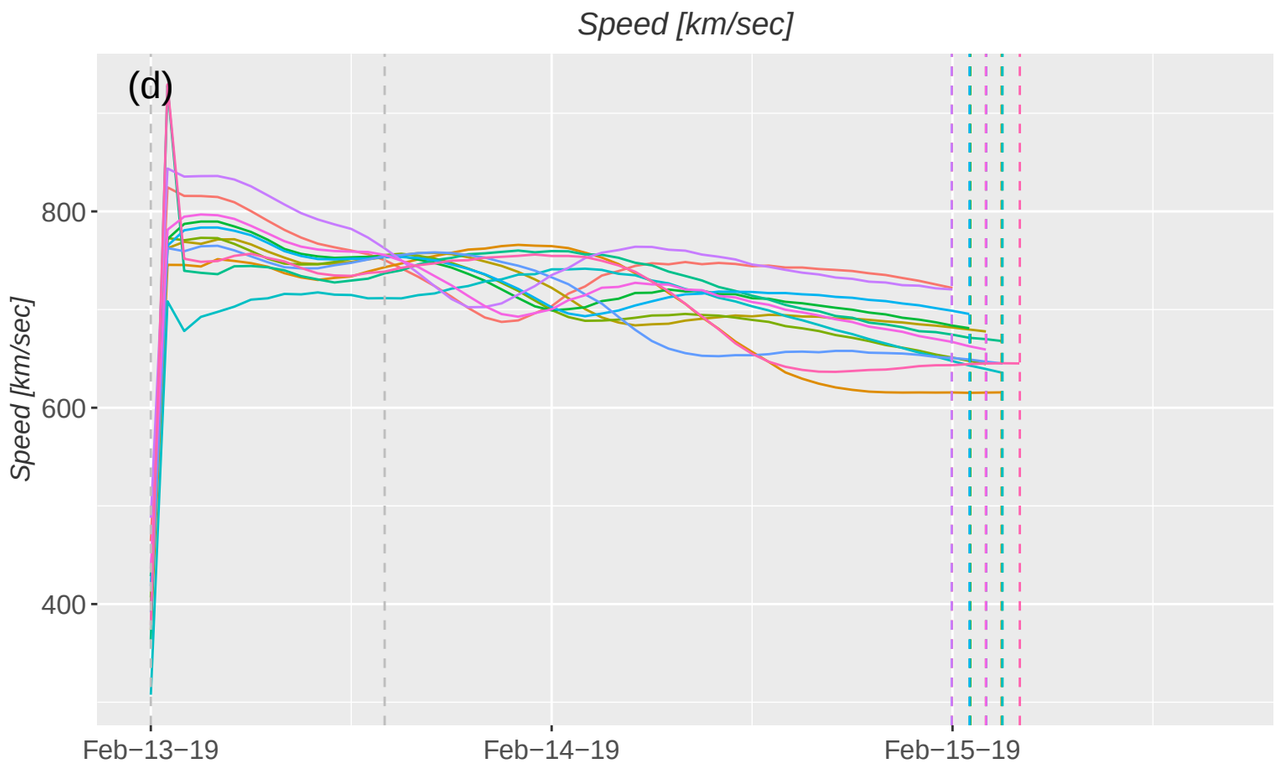
Speed [km/sec]
(d)
800
600
400
Speed [km/sec]
Feb−13−19
Feb−14−19
Feb−15−19

Figure.

ADAPT MAP # 1

ADAPT MAP # 2

ADAPT MAP # 3

ADAPT MAP # 4

ADAPT MAP # 5

ADAPT MAP # 6

ADAPT MAP # 7

ADAPT MAP # 8

ADAPT MAP # 9

ADAPT MAP # 10

ADAPT MAP # 11

ADAPT MAP # 12

count

Arrival Time [hours]

Figure.

Speed [km/sec]

(a)

900
700
500
300

Speed [km/sec]

Feb–13–19
Feb–14–19
Feb–15–19
Feb–16–19
Feb–17–19
Feb–18–19
Feb–19–19
Feb–20–19

Magnetic Field Magnitude [nT]

(b)

6
4
2
0

Magnetic Field Magnitude [nT]

Feb–13–19
Feb–14–19
Feb–15–19
Feb–16–19
Feb–17–19
Feb–18–19
Feb–19–19
Feb–20–19

Temperature [K]

(c)

4e+05
3e+05
2e+05
1e+05

Temperature [K]

Feb–13–19
Feb–14–19
Feb–15–19
Feb–16–19
Feb–17–19
Feb–18–19
Feb–19–19
Feb–20–19

Density [1/cm^3]

(d)

200
150
100
50
0

Density [1/cm^3]

Feb–13–19
Feb–14–19
Feb–15–19
Feb–16–19
Feb–17–19
Feb–18–19
Feb–19–19
Feb–20–19

Figure.

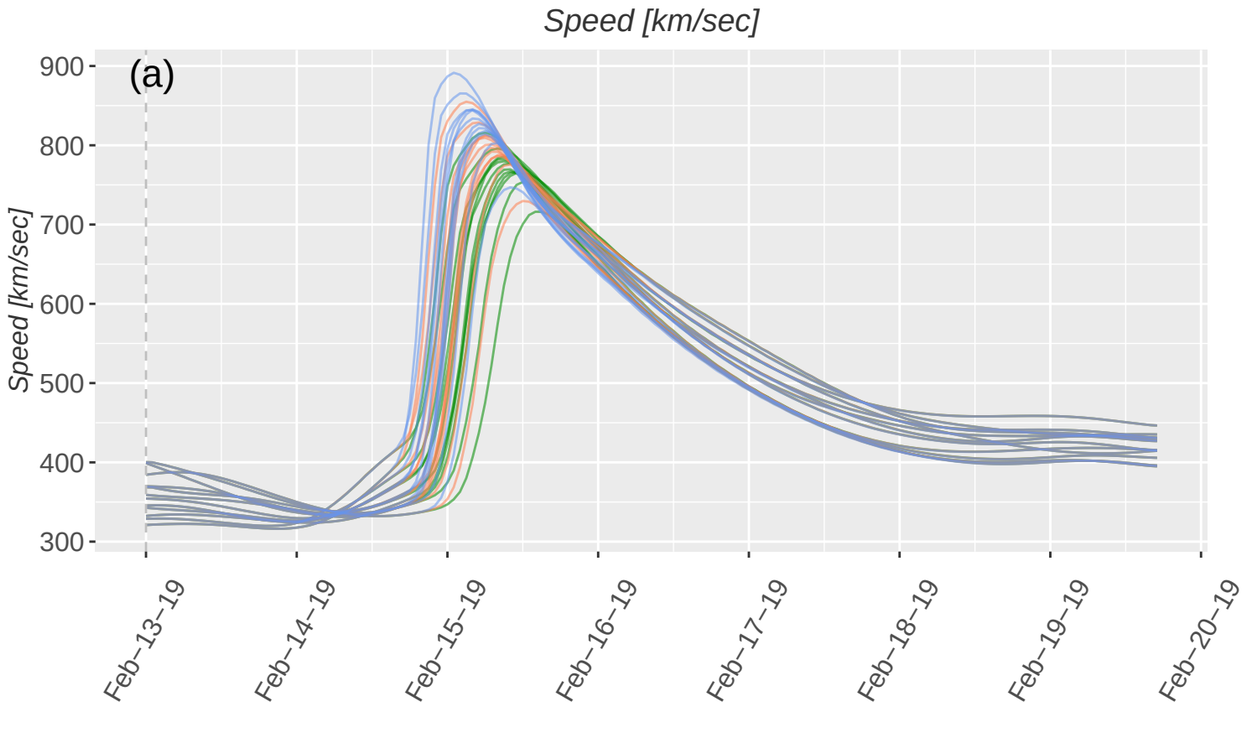
Speed [km/sec]
(a)
900
800
700
600
500
400
300
Speed [km/sec]
Feb–13–19
Feb–14–19
Feb–15–19
Feb–16–19
Feb–17–19
Feb–18–19
Feb–19–19
Feb–20–19

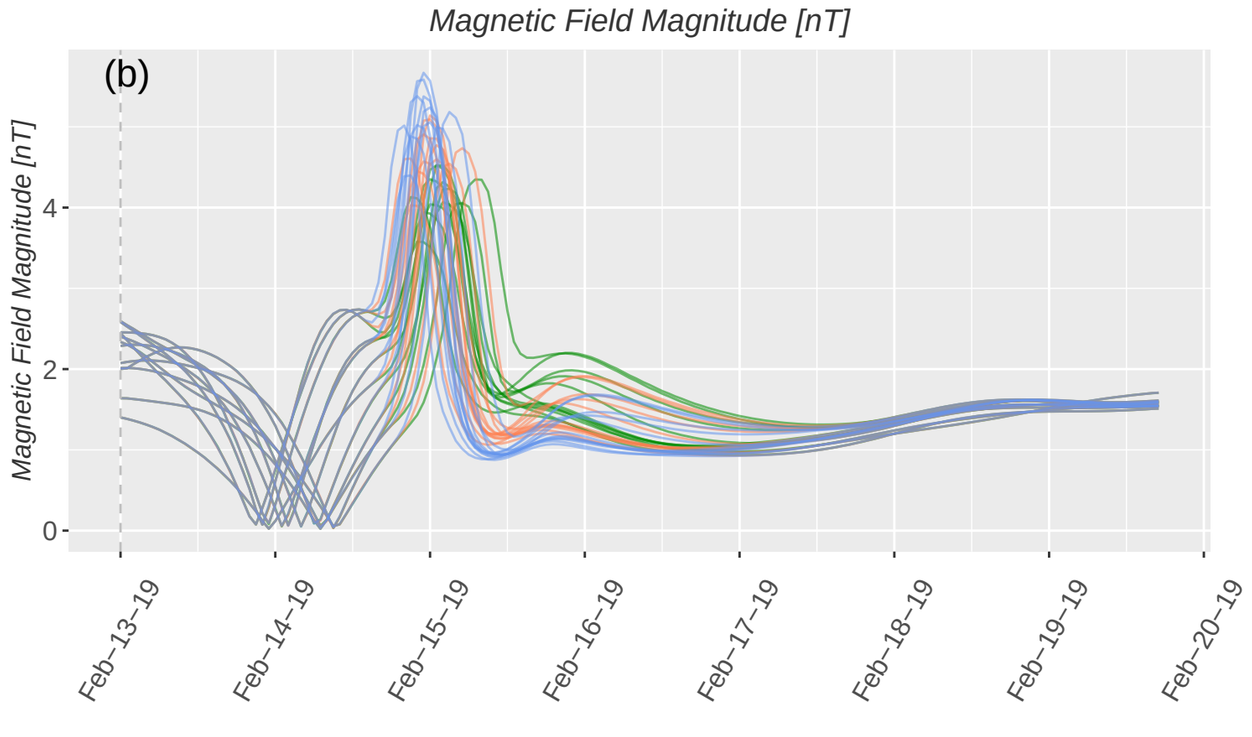
Magnetic Field Magnitude [nT]
(b)
4
2
0
Magnetic Field Magnitude [nT]
Feb–13–19
Feb–14–19
Feb–15–19
Feb–16–19
Feb–17–19
Feb–18–19
Feb–19–19
Feb–20–19

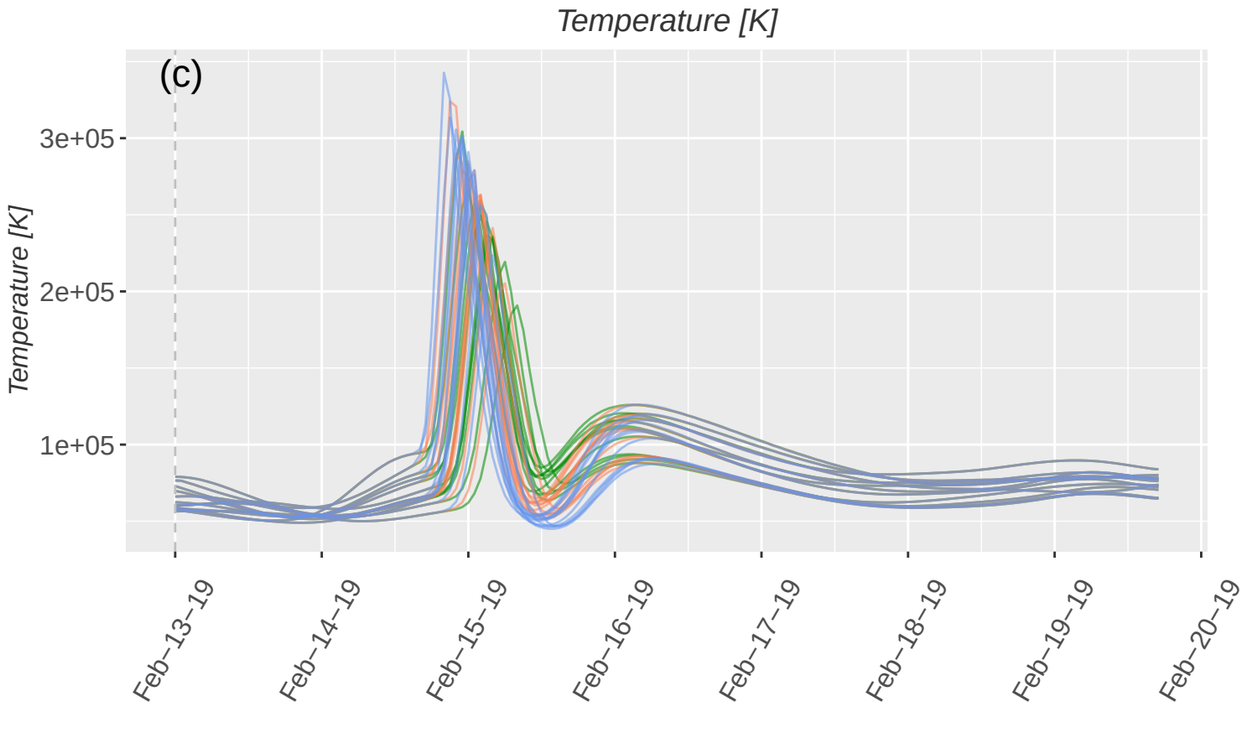
Temperature [K]
(c)
3e+05
2e+05
1e+05
Temperature [K]
Feb–13–19
Feb–14–19
Feb–15–19
Feb–16–19
Feb–17–19
Feb–18–19
Feb–19–19
Feb–20–19

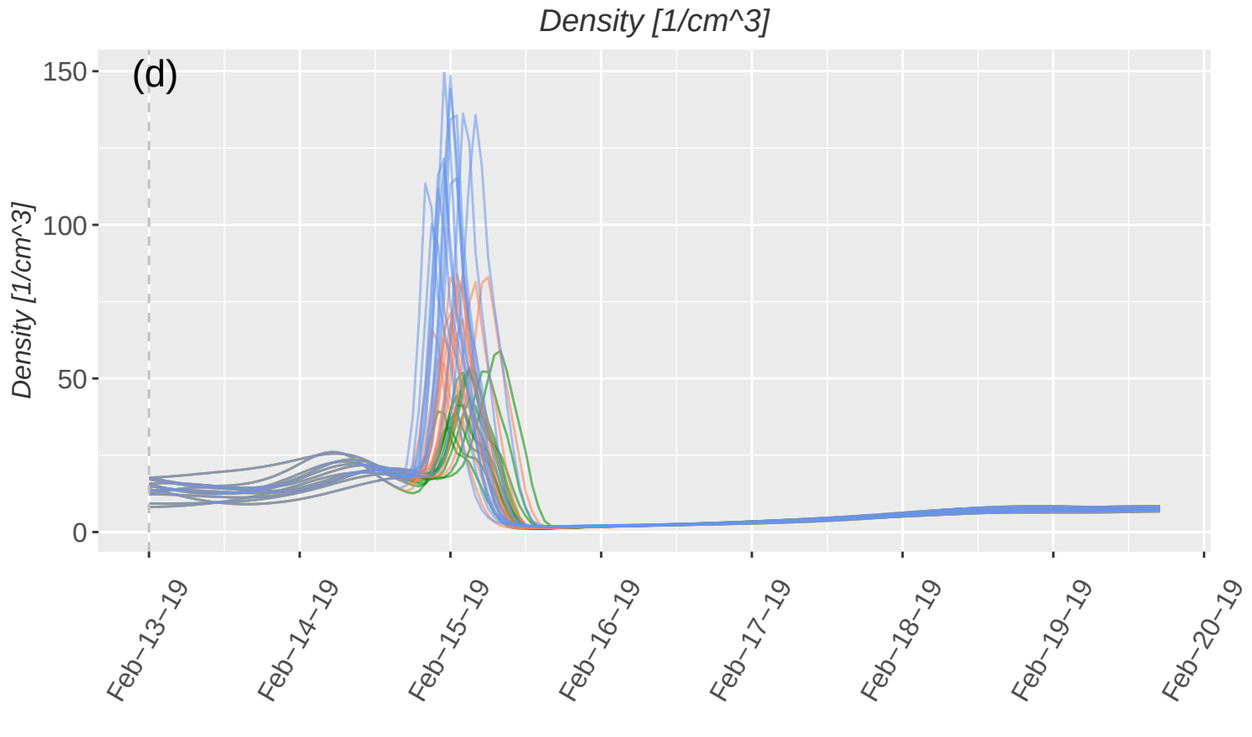
Density [1/cm^3]
(d)
150
100
50
0
Density [1/cm^3]
Feb–13–19
Feb–14–19
Feb–15–19
Feb–16–19
Feb–17–19
Feb–18–19
Feb–19–19
Feb–20–19